Mass loss from inhomogeneous hot star winds

I. Resonance line formation in 2D models

J.O. Sundqvist[1], J. Puls[1], and A. Feldmeier[2]

[1] Universitätssternwarte München, Scheinerstr. 1, 81679 München, Germany
   e-mail: jon@usm.uni-muenchen.de
[2] Institut für Physik und Astronomie, Karl-Liebknecht-Strasse 24/25, 14476 Potsdam-Golm, Germany

ABSTRACT

Context. The mass-loss rate is a key parameter of hot, massive stars. Small-scale inhomogeneities (clumping) in the winds of these stars are conventionally included in spectral analyses by assuming optically thin clumps, a void inter-clump medium, and a smooth velocity field. To reconcile investigations of different diagnostics (in particular, unsaturated UV resonance lines vs. H_α/radio emission) within such models, a highly clumped wind with very low mass-loss rates needs to be invoked, where the resonance lines seem to indicate rates an order of magnitude (or even more) lower than previously accepted values. If found to be realistic, this would challenge the radiative line-driven wind theory and have dramatic consequences for the evolution of massive stars.
Aims. We investigate basic properties of the formation of resonance lines in small-scale inhomogeneous hot star winds with non-monotonic velocity fields.
Methods. We study inhomogeneous wind structures by means of 2D stochastic and pseudo-2D radiation-hydrodynamic wind models, constructed by assembling 1D snapshots in radially independent slices. A Monte-Carlo radiative transfer code, which treats the resonance line formation in an axially symmetric spherical wind (without resorting to the Sobolev approximation), is presented and used to produce synthetic line spectra.
Results. The optically thin clumping limit is only valid for very weak lines. The detailed density structure, the inter-clump medium, and the non-monotonic velocity field are all important for the line formation. We confirm previous findings that radiation-hydrodynamic wind models reproduce observed characteristics of strong lines (e.g., the black troughs) without applying the highly supersonic 'microturbulence' needed in smooth models. For intermediate strong lines, the velocity spans of the clumps are of central importance. Current radiation-hydrodynamic models predict spans that are too large to reproduce observed profiles unless a very low mass-loss rate is invoked. By simulating lower spans in 2D stochastic models, the profile strengths become drastically reduced, and are consistent with higher mass-loss rates. To simultaneously meet the constraints from strong lines, the inter-clump medium must be non-void. A first comparison to the observed Phosphorus V doublet in the O6 supergiant λ Cep confirms that line profiles calculated from a stochastic 2D model reproduce observations with a mass-loss rate approximately ten times higher than that derived from the same lines but assuming optically thin clumping. Tentatively this may resolve discrepancies between theoretical predictions, evolutionary constraints, and recent derived mass-loss rates, and suggests a re-investigation of the clump structure predicted by current radiation-hydrodynamic models.

Key words. stars: early-type - stars: mass-loss - radiative transfer - line: formation - hydrodynamics - instabilities

1. Introduction

Mass loss through supersonic stellar winds is pivotal for the physical understanding of hot, massive stars and their surroundings. A change of only a factor of two in the mass-loss rate has a dramatic effect on massive star evolution (Meynet et al. 1994). Winds from these stars are described by the line-driven wind theory (Castor et al. 1975; Pauldrach et al. 1986), which traditionally assumes the wind to be stationary, spherically symmetric, and homogeneous. Despite this theory's apparent success (e.g., Vink et al. 2000), evidence for an inhomogeneous and time-dependent wind has over the past years accumulated, recently summarized in the proceedings from the workshop 'Clumping in hot star winds' (Hamann et al. 2008) and in a general review of mass loss from hot, massive stars (Puls et al. 2008b).

That line-driven winds should be intrinsically unstable was already pointed out by Lucy & Solomon (1970), and was later confirmed first by linear stability analyses and then by direct, radiation-hydrodynamic modeling of the time-dependent wind (e.g., Owocki & Rybicki 1984; Owocki et al. 1988; Feldmeier 1995; Dessart & Owocki 2005), where the line-driven (or line-deshadowing) instability causes a small-scale, inhomogeneous wind in both density and velocity.

Direct observational evidence of a small-scale, clumped stellar wind has, for O-stars, so far only been given for two objects, ζ Pup and HD 93129A (Eversberg et al. 1998; Lépine & Moffat 2008). Much *indirect* evidence, however, has arisen from quantitative spectroscopy, where the standard way of deriving mass-loss rates from observations nowadays is via line-blanketed, non-LTE (LTE: local thermodynamic equilibrium) model atmospheres that include a treatment of both the photosphere and the wind. Wind clumping has been included in such codes (e.g., CMFGEN (Hillier & Miller 1998), PoWR (Gräfener et al. 2002), FASTWIND (Puls et al. 2005)) by assuming statistically distributed *optically thin* density clumps and a void inter-clump medium, while keeping the smooth velocity law. The major result from this methodology is that any mass-loss rate derived from smooth models and density-squared diagnostics (H_α, infra-red and radio emission) needs to be scaled down by the

square root of the clumping factor (which describes the over density of the clumps as compared to the mean density, see Sect. 2.2). For example, Crowther et al. (2002), Bouret et al. (2003), and Bouret et al. (2005) have concluded that a reduction of 'smooth' mass-loss rates by factors 3 . . . 7 might be necessary. Furthermore, from a combined optical/IR/radio analysis of a sample of Galactic O-giants/supergiants, Puls et al. (2006) derived upper limits on observed rates that were factors of 2 . . . 3 lower than previous H_α estimates based on a smooth wind.

On the other hand, the strength of UV resonance lines ('P Cygni lines') in hot star winds depends linearly on the density and is therefore not believed to be directly affected by optically thin clumping. By using the Sobolev with exact integration technique (SEI; cf. Lamers et al. 1987) on the unsaturated Phosphorus V (PV) lines, Fullerton et al. (2006) for a large number of Galactic O-stars derived rates that were factors of 10 . . . 100 lower than corresponding smooth H_α/radio values (provided PV is the dominant ion in spectral classes O4 to O7). Such large revisions would conflict with the radiative line-driven wind theory and have dramatic consequences for the evolution of, and the feedback from, massive stars (cf. Smith & Owocki 2006; Hirschi 2008). Indeed, a puzzling picture has emerged, and it appears necessary to ask whether the present treatment of wind clumping is sufficient. Particularly the assumptions of optically thin clumps, a void inter-clump medium, and a smooth velocity field may not be adequate to infer proper rates under certain conditions.

Optically thin vs. optically thick clumps. Oskinova et al. (2007) used a porosity formalism (Feldmeier et al. 2003; Owocki et al. 2004) to scale the opacity from smooth models and investigate impacts from *optically thick* clumps on the line profiles of ζ Pup. Due to a reduction in the effective opacity, the authors were able to reproduce the PV lines without relying on a (very) low mass-loss rate, while simultaneously fitting the optically thin H_α line. This formalism, however, was criticized by Owocki (2008) who argued that the original porosity concept had been developed for continuum processes, and that line transitions rather should depend on the non-monotonic velocity field seen in hydrodynamic simulations. Proposing a simplified analytic description to account for this velocity-porosity, or 'vorosity', he showed how also this effect may reduce the effective opacity.

In this first paper we attempt to clarify the most important concepts by conducting a detailed investigation on the synthesis of UV resonance lines from inhomogeneous two-dimensional (2D) winds. We create both pseudo-2D, radiation-hydrodynamic wind models and 2D, stochastic wind models, and produce synthetic line profiles via Monte-Carlo radiative transfer calculations. We account for and analyze the effects from a wind clumped in *both* density and velocity as well as the effects from a non-void inter-clump medium. Especially we focus on lines with intermediate line strengths, comparing the behavior of these lines with the behavior of both optically thin lines and saturated lines. Follow-up studies will include a treatment of emission lines (e.g., H_α) and an extension to 3D, and the development of simplified approaches to incorporate effects into non-LTE models.

In Sect. 2 we describe the wind models and in Sect. 3 the Monte-Carlo radiative transfer code. First results from 2D inhomogeneous winds are presented in Sect. 4, and an extensive parameter study is carried out in Sect. 5. We discuss some aspects of the interpretations of these results and perform a first compar-ison to observations in Sect. 6, and summarize our findings and outline future work in Sect. 7.

2. Wind models

For wind models, we use customary spherical coordinates (r, Θ, Φ) with r the radial coordinate, Θ the polar angle, and Φ the azimuthal angle. We assume spherical symmetry in 1D models and symmetry in Φ in 2D models. In all 2D models Θ is sliced into N_Θ equally sized slices, giving a lateral scale of coherence (or an opening angle) $180/N_\Theta$ degrees. This 2D approximation is discussed in Sect. 6.4. Below we describe the model types primarily used in the present analysis; two are of stochastic nature and two are of radiation-hydrodynamic nature.

2.1. Radiation-hydrodynamic wind models

We use the time-dependent, radiation-hydrodynamic (hereafter RH) wind models from Puls et al. (1993, hereafter 'POF'), calculated by S. Owocki, and from Feldmeier et al. (1997, hereafter 'FPP'), and the reader is referred to these papers for details. Here we summarize a few important aspects. POF assume a 1D, spherically symmetric outflow, and circumvent a detailed treatment of the wind energy equation by assuming an isothermal flow. Perturbations are triggered by photospheric sound waves. The wind consists of 800 radial points, extending to roughly 5 stellar radii. FPP also assume a 1D, spherically symmetric outflow, but include a treatment of the energy equation. Perturbations are triggered either by photospheric sound waves or by Langevin perturbations that mimic photospheric turbulence. The wind consists of 4000 radial points, extending to roughly 30 stellar radii. Tests have shown that the FPP winds yield similar results for both flavors of perturbations, and, for simplicity, we therefore use only the results of the turbulence model.

Due to the computational cost of obtaining the line force, only initial attempts to 2D RH simulations have been carried out (Dessart & Owocki 2003, 2005). These authors first used a strictly radial line force, yielding a complete lateral incoherent structure due to Rayleigh-Taylor or thin-shell instabilities, and in the follow-up study uses a restricted 3-ray approach to approximate the lateral line drag, yielding a larger lateral coherence but lacking quantitative results. Therefore, and because of the general dominance of the radial component in the radiative driving, we create fragmented 2D wind models from our 1D RH ones by assembling snapshots in the Θ direction, assuming independence between each slice consisting of a pure radial flow. After the polar angle has been sliced into N_Θ equally sized slices, one random snapshot is selected to represent each slice. This method for creating more-D models from 1D ones is essentially the same as the 'patch method' used by Dessart & Owocki (2002), when synthesizing emission lines for Wolf-Rayet stars, and the method used by, e.g., Oskinova et al. (2004), when synthesizing X-ray line emission from stochastic wind models. Fig. 1 displays typical velocity and density structures from this type of 2D model.

2.2. Stochastic wind models

We also study clumpy wind structures created by means of distorting a smooth, stationary, and spherically symmetric wind via stochastic procedures. This allows us to investigate the impacts from, and to set constraints on, different key parameters without being limited by the values predicted by the RH simula-
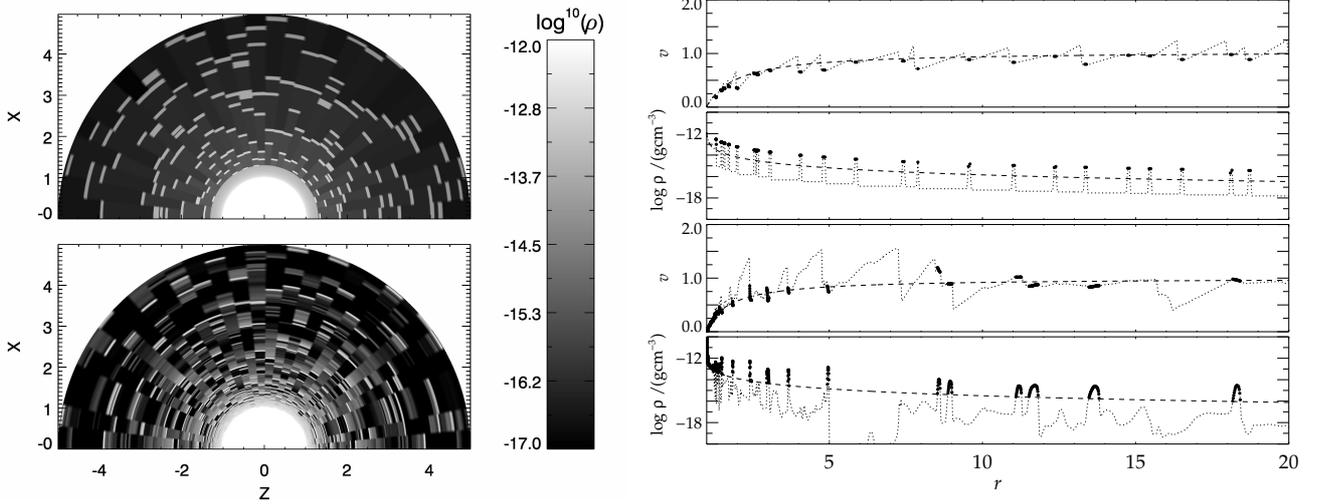
Fig. 1. *Left panel:* Density contour plots of one stochastic (upper plot) and one RH (FPP, lower plot) model. The Cartesian coordinate Z is on the abscissa and X is on the ordinate. *Right panel:* Density and velocity structures of one slice in one stochastic (upper) and one RH (FPP, lower) model. Over densities are marked with filled dots. For model parameters and details, see Sect. 2.2.

tions. For the underlying smooth winds we adopt a standard β velocity law $v_\beta(r) = (1 - b/r)^\beta$. Here and throughout the paper, we measure *all* velocities in units of the terminal velocity, v_∞, and *all* distances and length scales in units of the stellar radius, $R_\star$. b is given by $v(r = 1) = v_{min}$, the velocity at the base of the wind. $v_{min} = 0.01$ is assumed, roughly corresponding to the sound speed. For a given $\dot{M}$, the homogeneous density structure then follows directly from the equation of continuity. We choose $\beta = 1$, which is appropriate for a standard O-star wind and allows us to derive simple analytic expressions for wind masses and flight times.

A model clumped in density. First we consider a two component density structure consisting of clumps and a rarefied interclump medium (hereafter ICM), but keep the $\beta = 1$ velocity law. Clumps are released randomly in radial direction at the inner boundary, independently from each slice. The release in radial direction means that a given clump stays within the same slice during its propagation through the wind. The average time interval between the release of two clumps is δt, which here and in the following is expressed in units of the wind's dynamic time scale $t_{dyn} = R_\star/v_\infty$.

The average distance between clumps thus is $v_\beta \, \delta t$, i.e. clumps are spatially closer in the inner wind than in the outer wind, and for example $\delta t = 0.5$ (in t_{dyn}) gives an average clump separation of 0.5 (in $R_\star$) at the point where $v = 1$ (in v_∞). We further assume that the clumps preserve mass and lateral angle when propagating outwards, and that the underlying model's total wind mass is conserved within every slice. This radial clump *distribution* is the same as the one used by Oskinova et al. (2006) when simulating X-ray emission from O-stars, but differs from the one used by Oskinova et al. (2007) when investigating porosity effects on resonance lines (see discussion in Sect. 6.5). The radial clump *widths* are here calculated from the actual wind geometry and clump distribution by assuming a *volume filling*

factor f_v, defined as the fractional volume of the dense gas[1]. A related quantity is the *clumping factor*

$$f_{cl} \equiv \frac{\langle \rho^2 \rangle}{\langle \rho \rangle^2}, \tag{1}$$

as defined by Owocki et al. (1988), where angle brackets denote temporal averages. Identifying temporal with spatial averages one may write for a two component medium (cf. Abbott et al. 1981)

$$f_{cl} = \frac{f_v + (1 - f_v)x_{ic}^2}{[f_v + (1 - f_v)x_{ic}]^2}, \tag{2}$$

with

$$x_{ic} \equiv \frac{\rho_{ic}}{\rho_{cl}}, \tag{3}$$

the ratio of low- to high-density gas (subscript ic denotes interclump and cl denotes clump). For a void ($x_{ic} = 0$) ICM, $\rho_{cl}/\langle \rho \rangle = f_v^{-1} = f_{cl}$, i.e, f_{cl} then describes the over density of the clumps as compared to the mean density.

A model clumped in density and velocity. Next we consider also a non-monotonic velocity law, using the spatial distribution and widths of the clumps described in the previous paragraph. The RH simulations indicate that, generally, strong shocks separate denser and slower material from rarefied regions with higher velocities. Building on this basic result, we now modify the velocity fields in our stochastic models by adding a random perturbation to the local v_β value prior to the starting point of each clump, so that the new velocity becomes v_{pre}. A 'jump velocity' is thereafter determined by a random subtraction from v_β, now using the added perturbation as the maximum subtraction. That is,

$$v_{pre} = v_\beta + v_j \times 2R_1 \qquad v_{post} = v_\beta - v_j \times 2R_1R_2, \tag{4}$$

---

[1] We here notice that f_v is normalized to the *total* volume, i.e., $f_v = 0 \ldots 1$. In some literature f_v is identified with the straight volume ratio V_{cl}/V_{ic}, which then implicitly assumes that $V_{cl} \ll V_{ic}$.

Table 1. Basic parameters defining a stochastic wind model clumped in density and with a non-monotonic velocity field.

Name	Parameter	Considered range
Volume filling factor	$f_{\rm v}$	$f_{\rm v}$ = 0.01 ... 1.0
Average time interval between release of clumps	δt	$\delta t\,[t_{\rm dyn}]$ = 0.05 ... 1.5
ICM density parameter, Eq. 3	$x_{\rm ic}$	$x_{\rm ic}$ = 0 ... 0.1
Velocity span of clump	δv	$\delta v/\delta v_\beta$ = −10.0 ... 1.0
Parameter determining the jump velocity	$v_{\rm j}$	$v_{\rm j}/v_\beta$ = 0.01 ... 0.15
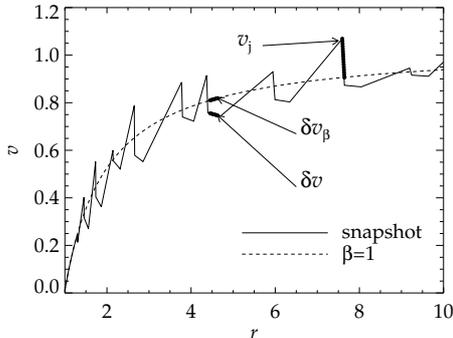
Fig. 2. Non-monotonic velocity field and corresponding parameters in a stochastic model.

where R_1 and R_2 are two random numbers in the interval 0 to 1. $v_{\rm pre} - v_{\rm post}$ is the jump velocity as determined by the parameter $v_{\rm j}$. By multiplying R_1 by two, we make sure that the mean perturbation at the 'pre' point is $v_{\rm j}$, and R_2 allows for an asymmetry about v_β (see Fig. 2). The clump is assumed to start at $v_{\rm post}$, and its velocity span is set by assuming a value for $\delta v/\delta v_\beta$, where δv is the velocity span of the clump and δv_β the corresponding quantity for the same clump with a smooth velocity law (see Fig. 2). Inspection of our RH models suggests that velocity gradients within density enhancements primarily are negative (see also Sect. 6.3), and negative gradients are also adopted in most of our stochastic models. Finally we assume a constant velocity gradient through the ICM.

Overall, the above treatment provides a phenomenological description of the non-monotonic velocity field seen in RH simulations. The description differs from the one suggested by Owocki (2008), who uses only one parameter to characterize the velocity field (whereas we have two). Our new formulation is motivated by both observational and modeling constraints from strong and intermediate lines, as discussed in Sect. 6.5.

The basic parameters defining a stochastic model are listed in Table 1. Fig. 1 (right panel) shows the density and velocity structures of one slice in a stochastic model, with density parameters $f_{\rm v} = 0.1$, $\delta t = 1.0$, $x_{\rm ic} = 0.005$, and velocity parameters $v_{\rm j} = 0.15 v_\beta$ and $\delta v = -\delta v_\beta$. Clump positions have been highlighted with filled dots and a comparison to a RH model (FPP) is given. In the RH model, we have identified clump positions by highlighting all density points with values higher than the corresponding smooth model. The left panel shows the density contours of the same models, where, for clarity, only the wind to $r = 5$ is displayed.

3. Radiative transfer

To compute synthetic line profiles from the wind models, we have developed a Monte-Carlo radiative transfer code (MC-2D)

that treats resonance line formation in a spherical and axially symmetric wind using an 'exact' formulation (e.g., without resorting to the Sobolev approximation). The restriction to 2D is of course a shortage, but has certain geometrical and computational advantages and should be sufficient for the study of general properties, as discussed in Sect. 6.4. A thorough description and verification of the code can be found in Appendix A.

Photons are released from the lower boundary (the photosphere) and each path is followed until the photon has either left the wind or been backscattered into the photosphere. Basic assumptions are a line-free continuum with no limb darkening emitted at the lower boundary, no continuum absorption in the wind, pure scattering lines, instantaneous re-emission, and no overlapping lines (i.e., singlets). These simplifying assumptions, except for doublet formation, are all believed to be of minor importance to the basic problem. By the restriction to singlet line formation we avoid confusion between effects on the line profiles caused by line overlaps and by other important parameters, but on the other hand it also prevents a direct comparison to observations for many cases (but see Sect. 6.6). A consistent treatment of doublet formation will be included in the follow-up study.

4. First results from 2D inhomogeneous winds

Throughout this section we assume a thermal velocity, $v_{\rm t} = 0.005$ (in units of v_∞ and ~ 10 km s^{-1}, appropriate for a standard O-star wind), and apply no microturbulence. After a brief discussion on the impact of the observer's position and opening angles, we concentrate on investigating the formation of strong, intermediate, and weak lines. In our definition, an intermediate line is characterized by a line strength[2] $\kappa_0 = 5.0$ chosen such as to almost precisely reach the saturation limit in a *smooth* model (cf. Fig. 3).

By investigating these different line types, we account for the tight constraints that exist for each flavor: i) *weak lines* should be independent of density-clumping properties as long as the clumps remain optically thin, ii) for *intermediate lines* either smooth models overestimate the profile strengths or mass-loss rates are lower than previously thought (e.g. the PV problem, see Sect. 1), and iii) *strong saturated lines* are clearly present in hot star UV spectra, and observed features need to be reproduced, such as high velocity ($> v_\infty$) absorption, the black absorption trough, and the reduction of re-emitted flux blueward of the line center.

4.1. Observer's position and opening angles

The observed spectrum as calculated from a 2D wind structure depends on the observer's placement relative to the star (see Appendix A). As it turns out, however, this dependence is relatively weak in both the stochastic and the RH models (the latter is demonstrated in the upper panel of Fig. 3). Tests have shown that the variability of the line profile's emission part is insignificant. The variability of the absorption part may be detectable, at least near the blue edge, but is still insignificant for the integrated profile strength; the equivalent width of the absorption part is almost independent of the observer's position. Also the opening angle, $180°/N_\Theta$, primarily has a smoothing effect on the profiles. In Fig. 3, prominent discrete absorption features appear

---

[2] with κ_0 proportional to the product of mass-loss rate and abundance of the considered ion, see Appendix A.
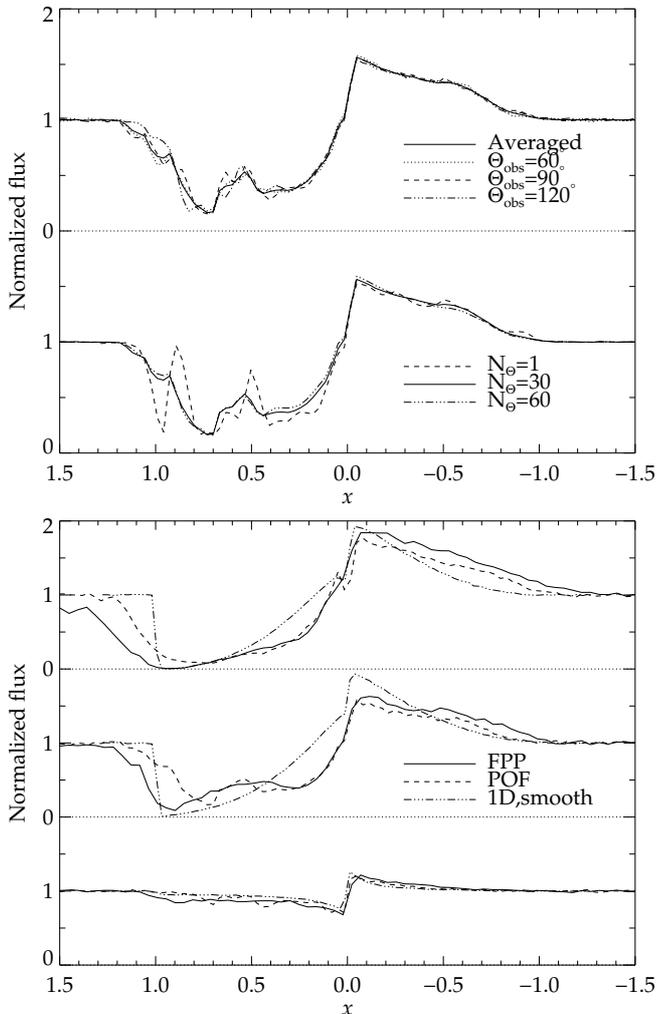
Fig. 3. Synthetic line profiles calculated from 2D RH models. The abscissa is the dimensionless frequency x (Eq. A.11), normalized to the terminal velocity, and the ordinate is the flux normalized to the continuum. *Upper panel:* Profiles from POF models with $\kappa_0 = 5.0$. The upper plot displays profiles for an observer placed at the Θ_{obs} angles as labeled in the figure and a profile averaged over all $N_\Theta = 30$ angles. The lower plot displays averaged profiles for three different N_Θ. *Lower panel:* Averaged profiles from FPP and POF models with $N_\Theta = 30$, and with $\kappa_0 = 100.0$ (upper) $\kappa_0 = 5.0$ (middle), and $\kappa_0 = 0.05$ (lower). For comparison, 1D, smooth profiles with the same values of κ_0 are shown as well.

near the blue edge in the model with $N_\Theta = 1$ (spherical symmetry), but are smoothed out in the 'broken-shell' models with $N_\Theta = 30$ and 60. The equivalent widths of the absorption parts are approximately equal for all three models.

Because our main interest here is the general behavior of the line profiles, we choose to work only with $N_\Theta = 30$ and profiles averaged over all observer angles from here on. Working with averaged line profiles has great computational advantages, because roughly a factor of N_Θ fewer photons are needed.

4.2. Radiation-hydrodynamic models

Fig. 3 (lower panel) shows line profiles from FPP and POF hydrodynamical models. For the strong lines, the constraints stated

in the beginning of this section are reproduced without adopting a highly supersonic and artificial microturbulence. These features arise because of the multiple resonance zones in a non-monotonic velocity field, and are present in spherically symmetric RH profiles as well (see POF for a comprehensive discussion); the main difference between 1D and 2D is a smoothing effect, partly stemming from averaging over all observer angles (see above). The absorption at velocities higher than the terminal is stronger in FPP than in POF, due to both a higher velocity dispersion and a larger extent of the wind ($r_{max} \sim 30$ as compared to $r_{max} \sim 5$, see Sect. 2.1); more overdense regions are encountered in the outermost wind, which (because of the flatness of the velocity field) leads to an increased probability to absorb at almost the same velocities.

For the intermediate lines, we again see the qualitative features of the strong lines, though less prominent. As compared to smooth models, a minor *absorption* reduction is present at velocities lower than the terminal, but compensated by the blue edge smoothing. Therefore the equivalent width of the line profile's absorption part in the FPP model is approximately equal to that of the smooth model, whereas in the POF model it is reduced by $\sim 10\%$. This minor reduction agrees with that found by Owocki (2008), and is not strong enough to explain the observations without having to invoke a very low mass-loss rate.

For the weak lines, the absorption part is marginally stronger than from a smooth, 1D model.

4.3. Stochastic models

In this subsection we use a 'default' 2D, stochastic model with parameters as specified in Table 2. By comparing this model to models in which one or more parameters are changed, we demonstrate key effects in the behavior of the line profiles.

Strong lines. For strong lines, the line profiles from the default model reproduce the observational constraints described in the first paragraph of this section. As in the RH models, we apply no microturbulence. Fig. 4 (left panels) demonstrates the importance of the ICM in the default model; the absorption part of a very strong line is not saturated when $x_{ic} = 0$. That is, with a void ICM we will, regardless of the opacity, always have line photons escaping their resonance zones without ever interacting with any matter, thereby de-saturating the line. This ICM finding agrees with that of Zsargó et al. (2008), who point out that a non-void ICM is crucial for the formation of highly ionized species such as O VI. We also notice that $\delta v = -\delta v_\beta$ (used in the default model) does not permit clumps to have velocities higher than the local v_β value, preventing absorption at velocities higher than the terminal one when the ICM is void.

Intermediate lines. For intermediate lines, the line profiles from the default model display the main observational requirement if to avoid a drastic reduction in 'smooth' mass-loss rates[3], namely a strong absorption reduction as compared to a smooth model. The left panels of Fig. 4 show how the integrated profile strength of the default model with $\kappa_0 = 5.0$ roughly corresponds to that of a smooth model having $\kappa_0 = 0.5$, i.e., the smooth model would result in a mass-loss rate (as estimated from the integrated profile strength) ten times *lower* than the clumped model. The figure also illustrates how the main effect is on the absorption

---

[3] Recall that $f_v = 0.25 \rightarrow f_{cl} \approx 4$, which implies $\dot{M} = \dot{M}_{smooth}/2$, if f_{cl} were derived from ρ^2-diagnostics assuming optically thin clumps.

Table 2. Primary stochastic wind models and parameters

Model name	f_v	δt [t_{dyn}]	x_{ic}	$\delta v / \delta v_\beta$	v_j / v_β	r_{st}[a]	r_{ext}[b]
Default	0.25	0.5	0.0025	-1.0	0.15	1.3	~25
RHcopy	0.1	0.5	0.005	-10.0	0.15	1.3	~5
Obs1	0.11	0.5,4.0[c]	0.005,0.0025[c]	-1.0	0.15	1.02	~25

[a] Radial onset of clumping. [b] Radial extent of wind.
[c] Left value inside the radius corresponding to $v_\beta = 0.6$, right value outside.
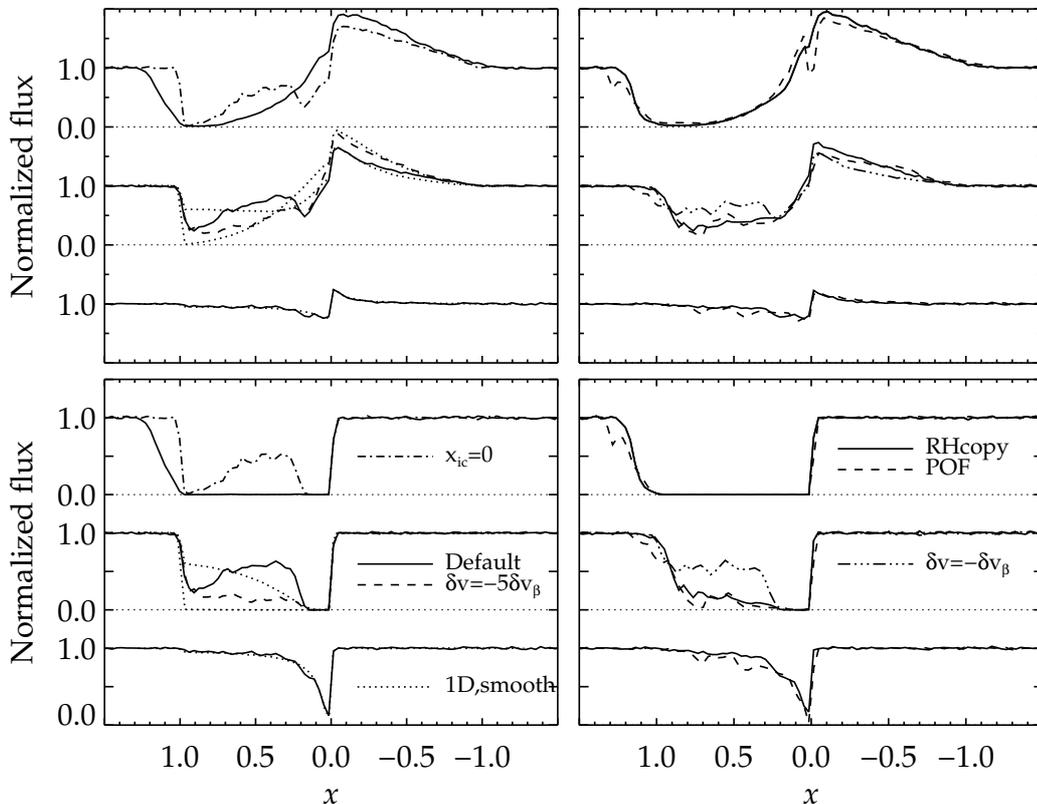
Fig. 4. *Left panels:* Solid lines display total line profiles and the absorption part for the default stochastic model (see Table 2), with $\kappa_0 = 1000$ (upper), $\kappa_0 = 5.0$ (middle), and $\kappa_0 = 0.05$ (lower). Dotted lines display smooth models with $\kappa_0 = 5.0$ and $\kappa_0 = 0.5$ (middle), and $\kappa_0 = 0.05$ (lower). Dashed/dashed-dotted lines with modifications from the default model as labeled in the figure. *Right panels:* Same as the left panels, but for POF (dashed lines) and RHcopy (solid lines). Dashed-dotted lines with modifications from RHcopy as labeled in the figure.

part of the line profile. In addition to the reduction in profile *strength*, the profile *shapes* of the absorption parts are noticeably different for the default and smooth models (the shapes of the re-emission parts, not shown here, are similar for the two models). We further discuss the shapes of the profiles in Sect. 6.1. The dramatic reduction in integrated profile strength occurs because of large velocity gaps between the clumps, in which the wind is unable to absorb (at this opacity the ICM may not 'fill in' these gaps with absorbing material).

We have identified $|\delta v|$ as a critical parameter for the formation of intermediate lines. The importance of the velocity spans of the clumps is well illustrated by the absorption part profiles in Fig. 4 (lower-left panel, middle plot). The absorption is much stronger in the comparison model with $\delta v = -5\delta v_\beta$ than in the default model with $\delta v = -\delta v_\beta$, because the former model covers more of the total velocity space *within* the clumps, thereby closing the gaps *between* the clumps. Consequently the wind may, on average, absorb at many more wavelengths.

In principle, however, this effect is counteracted by a decrease in the clump's optical depths, because of the now higher velocity gradients ($|\delta v / \delta v_\beta| > 1$). Consider the *radial* Sobolev optical depth (proportional to $\rho/|\partial v/\partial r|$, see Appendix A) in a stochastic wind model. As compared to a smooth model, the density inside a clump is enhanced by a factor of f_v^{-1} (assum-

ing a negligible ICM), but also the velocity gradient is enhanced by a factor of $|\delta v / \delta v_\beta|$. Thus we may write for the radial Sobolev optical depth inside a clump,

$$\tau_{Sob} \approx \frac{\tau_{Sob,sm}}{f_v |\delta v / \delta v_\beta|} \approx \frac{\kappa_0}{v_\beta f_v |\delta v / \delta v_\beta|}, \tag{5}$$

where 'sm' indicates a quantity from a smooth wind, and the expression to the right is valid for an underlying $\beta = 1$ velocity law. From Eq. 5, we see how the effects on the optical depth from the increased density ($f_v = 0.25$) and the increased velocity gradients ($|\delta v / \delta v_\beta| = 5$) almost cancel each other in this example. Thus, the clumps are still optically thick for the intermediate line ($\kappa_0 = 5$), which means that the larger coverage of the total velocity space 'wins', and the net effect becomes an increase in absorption (as seen in Fig. 4, lower-left panel, middle plot). This will be true as long as not $f_v |\delta v / \delta v_\beta| \gg 1$, which is never the case in the parameter range considered here.

Finally, the prominent absorption dip toward the blue edge in the default model turns out to be a quite general feature of our stochastic models, and is discussed in Sects. 5.1 and 6.2.

Weak lines. The statistical treatment of density clumping included in atmospheric codes such as CMFGEN, PoWR, and
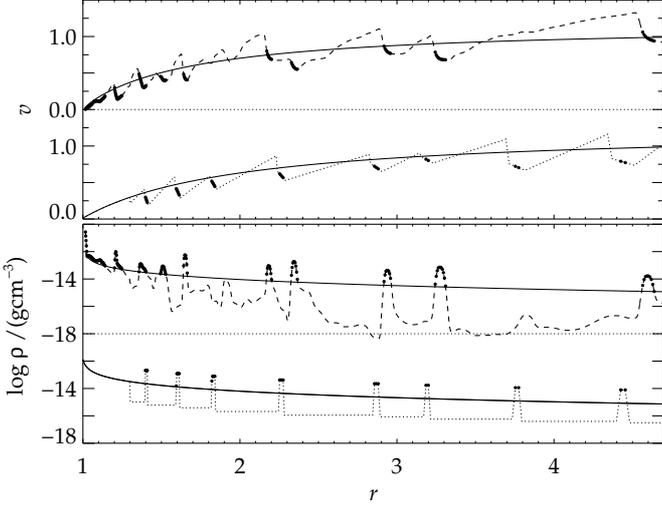
Fig. 5. Velocity (*upper panel*) and density (*lower panel*) structures for one slice in POF (dashed) and RHcopy (dotted), see Table 2. Solid lines are the corresponding smooth structures, and clumps are highlighted as in Fig. 1.

FASTWIND is valid for optically thin clumps and a negligible ICM, and gives no direct effect on resonance lines scaling linearly with density. Here we test this prediction using detailed radiative transfer[4]. Our default model recovers the smooth results when $\kappa_0 = 0.05$ (Fig. 4, left panels), confirming the expected behavior. However, from calculating spectra using different values of κ_0, we have found that significant deviations from smooth models occur for the default model already before κ_0 reaches unity. This occurs because the clumps start to become optically thick, which may again be understood by considering the radial Sobolev optical depth (Eq. 5). With $f_v \leq 0.25$ and $\kappa_0 \geq 0.25$, one finds $\tau_{\rm Sob} \geq 1.0$.

4.4. Comparison between stochastic and radiation-hydrodynamic models

Our stochastic wind models have been constructed to contain all essential ingredients of the RH models. Therefore they should also reproduce the RH results, at least qualitatively, if a suitable parameter set is chosen. To test this we used the POF model. In this model, the clumping factor increases drastically at $r \sim 1.3$, from $f_{\rm cl} \sim 1.0$ to $f_{\rm cl} \sim 10$, after which it stays basically constant. The average clump separation in the outer wind is roughly half a stellar radius. Important for the velocity field is that the velocity spans of the clumps are generally *larger* than corresponding 'β spans', i.e., $|\delta v/\delta v_\beta| > 1$ (this is the case in FPP as well), a characteristic behavior that primarily affects the intermediate lines (details will be discussed in Sect. 6.3). Finally, a suitable $v_{\rm j}$ can be assigned from the position of the blue edge in a strong line calculated from POF. Table 2 (entry RHcopy) summarizes all parameters used to create this stochastic, 'pseudo-RH' model. Fig. 5 displays one slice of the velocity and density structures in the POF and RHcopy models, and Fig. 4 (right panels) displays the line profiles.

The line profiles of POF are matched reasonably well by RHcopy. The intermediate lines again demonstrate the importance of the velocity spans of the clumps; for an alternative

---

[4] The *indirect* effect through the feedback on the occupation numbers is not included, because in this section we assume constant ionization.
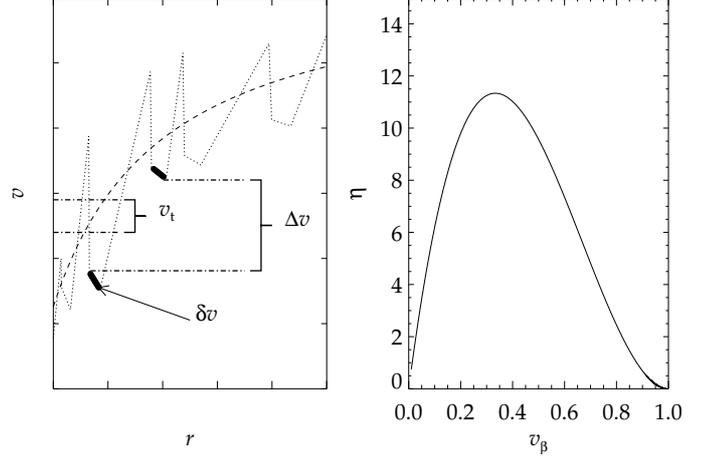
Fig. 6. *Left:* Schematic of Δv, the velocity gap between two subsequent clumps, made up by velocities not covered by *any* of the clumps. δv is the velocity span of a clump and $v_{\rm t}$ the thermal velocity. *Right:* The effective escape ratio η (Eq. 7) as a function of $\beta = 1$ velocity, for the parameters of the default model (see Table 2).

model with $\delta v = -\delta v_\beta$, there is much less absorption in the stochastic model than in POF, i.e., we encounter the same effect as discussed in the previous subsection. We conclude that in RH models it is the large velocity spans inside the density enhancements that prevent a reduction in profile strength (as compared to smooth models) for intermediate lines.

5. Parameter study

Having established basic properties, we now use our stochastic models to analyze the influence from different key parameters in more detail. First, however, we introduce a quantity that turns out to be particularly useful for our later discussion.

5.1. The effective escape ratio

For the important intermediate lines, it is reasonable to assume that the clumps are optically thick and the ICM negligible (see Sect. 4.3 and the next paragraph). Under these assumptions, a decisive quantity for photon absorption will be the velocity gap *not* covered by the clumps, as compared to the thermal velocity (the latter determining the width of the resonance zone in which the photon may interact with the wind material). This is illustrated in the left panel of Fig. 6, and we shall call this quantity the 'effective escape ratio'

$$\eta \equiv \frac{\Delta v}{v_{\rm t}}, \tag{6}$$

where Δv is the velocity gap between two subsequent clumps, made up by all velocities not covered by *any* of the clumps (see Fig. 6). In principle, η determines to which extent the vorosity effect (i.e., the velocity gaps between the clumps, cf. Owocki 2008) is important for the line formation. As defined, η does not contain any assumptions on the *spatial* structure of the wind. $\eta \ll 1$ means that the velocity gaps between the clumps are much smaller than the thermal velocity, which in turn means that the probability for a photon to encounter a clump within its resonance zone is high. If we assume each clump to be optically

thick, every encounter will lead to an absorption. Thus the probability for photon absorption is high when the value of η is low. Vice versa, $\eta >> 1$ results in a high probability for the photon to escape its resonance zone without interacting with the wind material, i.e., a low absorption probability. If the entire velocity space were covered by clumps, $\eta = 0$.

For the wind geometry used in our stochastic models, we may write (see Appendix B for a derivation)

$$\eta \approx \frac{v_\beta \delta t (1 - f_v |\delta v / \delta v_\beta|)}{L_r} \approx \frac{\delta t (1 - f_v |\delta v / \delta v_\beta|)}{v_t} \frac{v_\beta}{r^2}, \tag{7}$$

where L_r is the radial Sobolev length of a smooth model, which for $\beta = 1$ is $L_r \approx v_t r^2$ (as usual, r and L_r in $R_\star$ and δt in t_{dyn}). Note that in Eq. 7 also the density-clumping parameters have entered the expression for η, illustrating that there is an intimate coupling with the *spatial* clumping parameters, even though the vorosity effect initially depends on velocity parameters alone. For example, consider a wind with clumps that follow a smooth β velocity law. By bringing the clumps spatially closer together (for example by decreasing δt), the velocity gaps between them decrease as well. Thus one may choose to describe the changed situation either in terms of a less efficient porosity, because of fewer 'density holes' in the resonance zone through which the photons can escape (as done by Oskinova et al. 2007), *or* in terms of a less efficient vorosity, because of smaller velocity gaps between the clumps. Of course, one may also obtain a lower velocity gap between the clumps by increasing the actual velocity spans inside the clumps, as simulated in our stochastic models when $|\delta v / \delta v_\beta| > 1$. This effect, leading to a rather low vorosity, has already been demonstrated to be at work in the RH models (Sect. 4.4).

Using the parameters of our default model, Fig. 6 (right panel) displays η as a function of velocity and shows that η increases rapidly in the inner wind, reaches a maximum at $v \approx 0.33$, and then drops in the outer wind. To compare this behavior with that of the line profiles, we can associate absorption at some frequency x_{obs} with the corresponding value of the velocity, because absorption occurs at $x_{obs} \approx \mu v \approx v$ (radial photons dominate). In the default model's absorption-part line profile (see Fig. 4, the middle plot in the lower-left panel), a strong de-saturation occurs directly after the clumping is set to start (at $r = 1.3$, $v \approx 0.23$), followed by a maximum at $x_{obs} \approx 0.35$, and finally an absorption dip toward the blue edge. The behavior of the line profile is thus well mapped by η, and we may explain the absorption dip as a consequence of the low value of η in the outer wind, which in turn stems from the slow variation of the velocity field (i.e., from radially extended resonance zones).

5.2. Density parameters

To isolate density-clumping effects, we use a smooth $\beta = 1$ velocity law in this subsection. Despite the smooth velocity field, there are still holes in velocity space (because of the density clumping, at the locations where the ICM is present), and the expression for η (Eq. 7) remains valid. Since a smooth velocity field corresponds to $\delta v = \delta v_\beta$, also the run of η is equal to the one displayed in Fig. 6. In this subsection we work only with integrated profile strengths (characterized by the equivalent width W_λ of the line's absorption part). The shapes of the line profiles are discussed in Sect. 6.1.

Fig. 7 shows W_λ as a function of κ_0, for smooth models as well as for stochastic models with and without a contributing ICM. The figure directly tells: i) The default model ($x_{ic} =$
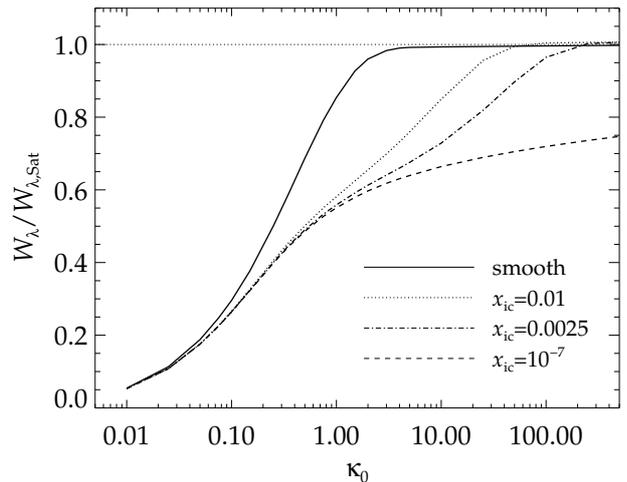
Fig. 7. Equivalent widths W_λ of the absorption parts of line profiles, normalized to the value of a saturated line, as a function of line strength parameter κ_0. The solid line is calculated from smooth models, and the dashed, dashed-dotted, and dotted lines from stochastic models with a smooth velocity field and $\delta t = 0.5$, $f_v = 0.25$, and x_{ic} as indicated.

0.0025) for the intermediate line ($\kappa_0 = 5.0$) displays a W_λ corresponding to a smooth model with a κ_0 roughly ten times lower. ii) Lines never saturate if the ICM is (almost) void. iii) The run of W_λ for the smooth and clumped models decouple well before κ_0 reaches unity. iv) For intermediate lines, the response of W_λ on variations of κ_0 is weak for clumped models. Points one to three confirm our findings from Sect. 4.3.

A variation of δt in the stochastic models affects primarily the high κ_0 part ($\kappa_0 \gtrsim 1.0$) of the curves in Fig. 7. For example, lowering δt in the model with a void ICM results in an upward shift of the dashed curve and vice versa. To obtain saturation with a void ICM, $\delta t \approx 0.05$ is required, which may be understood in terms of Eq. 7. For $\delta t = 0.05$, the η-values corresponding to the default model are decreased by a factor of ten, and η reaches a maximum of only about unity, with even lower values for the majority of the velocity space (cf. Fig. 6, right panel). The velocity gaps between the clumps then become closed, and the line saturates. In this situation, however, the intermediate line becomes saturated as well, again demonstrating the necessity of a *non-void* ICM to simultaneously saturate a strong line and not saturate an intermediate line. Only a properly chosen x_{ic} parameter ensures that the velocity gaps between the clumps become filled by low-density material able to absorb at strong line opacities, but *not* (or only marginally) at opacities corresponding to intermediate lines.

When varying x_{ic}, the primary change occurs at the high κ_0 end of Fig. 7. For higher (lower) values of x_{ic}, this part becomes shifted to the left (right), and the curve decouples earlier (later) from the corresponding curve for the void ICM. A higher ICM density obviously means that the ICM starts absorbing photons at lower line strengths and vice versa. Thus, observed saturated lines could potentially be used to derive the ICM density (or at least to infer a lower limit), *if* the mass-loss rate (and abundance) is known from other diagnostics.

The behavior of the absorption with respect to the volume filling factor is as expected from the expression for η; the higher f_v, the lower the value of η, and the stronger the absorption. This is because a higher f_v for a fixed δt implies that the clumps be-

come more extended, whereas the distances between clump centers remain unaffected. Consequently, a larger fraction of the total wind velocity is covered by the clumps, leading to stronger absorption. For weak lines ($\kappa_0 \approx 0.05$), the ratio $W_\lambda/W_{\lambda,sm}$ deviates significantly from unity only when $f_v \lesssim 0.1$. Only for such low values can high enough clump densities be produced so that the clumps start to become optically thick.

From Fig. 7 it is obvious that, generally, clumped models have a different (slower) response in W_λ to an increase in κ_0 than do smooth models. This behavior may be observationally tested using UV resonance doublets (Massa et al. 2008), because the only parameter that differs between the two line components is the oscillator strength. Thus, if a smooth wind model is used and the fitted ratio of line strengths (i.e., $\kappa_{0,blue}/\kappa_{0,red}$) does not correspond to the expected ratio of oscillator strengths, one may interpret this as a signature of a clumped wind. Such behavior was found by Massa et al. (2008), where the observed ratios of the blue to red component of Si IV $\lambda\lambda1394,1403$ in B supergiants showed a wide spread between unity and the expected factor of two. This result indicates precisely the slow response to an increase in κ_0 that is consistent with inhomogeneous wind models such as those presented here, but not with smooth ones. In inhomogeneous models, the expected profile strength (or W_λ) ratio between two doublet components will depend on the adopted clumping parameters (as demonstrated by Fig. 7 and the discussion above) and may in principle take any value in the range found by Massa et al.. That is, while a profile-strength ratio deviating from the value expected by smooth models might be a clear indication of a clumped wind, the opposite is not necessarily an indication of a smooth wind. Furthermore, the degeneracy between a variation of clumping parameters and κ_0 suggests that un-saturated resonance lines should be used primarily as consistency tests for mass-loss rates derived from other diagnostics rather than as direct mass-loss estimators. We will return to this problem in Sect. 6.6, where a first comparison to observations is performed for the PV doublet.

5.3. Velocity parameters

The jump velocity parameter, v_j, affects only the strong lines (or, more specifically, the lines for which the ICM is significant), and determines the maximum velocity at which absorption can occur. For example, by setting $v_j = 0$, no absorption at frequencies higher than $x = 1$ is possible (unless δv is positive and very high). A higher v_j also implies more velocity overlaps, and thereby an increased amount of backscattering due to multiple resonance zones. Both effects are illustrated in Fig. 8. Judging from the line profiles of the lower panel, the blue edge and the reduction of the re-emitted flux blueward of the line center may both be used to constrain v_j. The upper panel shows one slice of the corresponding velocity fields, illustrating that the underlying β law is recovered almost perfectly when using $v_j = 0.01v_\beta$ and $\delta v = \delta v_\beta$. With this velocity law and a non-void ICM, the corresponding strong line profile is equivalent to a profile from a smooth model.

In Sects. 4.3 and 4.4, we showed that a higher value of the clumps' velocity spans led to stronger absorption for intermediate lines. In principle this is as expected from Eq. 7, where η always decreases with increasing $|\delta v/\delta v_\beta|$. However, with the very high value of $|\delta v/\delta v_\beta|$ used in, e.g., the RHcopy model, one realizes that η in Eq. 7 becomes identically zero, because $f_v|\delta v/\delta v_\beta| = 1$. An $\eta = 0$ corresponds to the whole velocity space being covered by clumps, and the saturation limit should
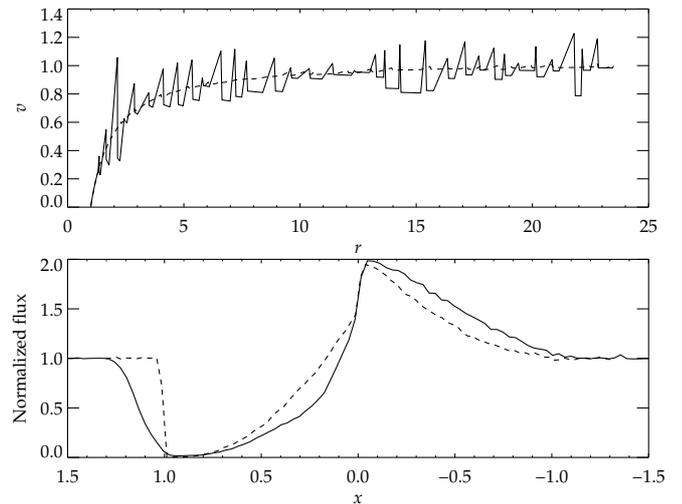
Fig. 8. *Upper:* Velocity structures (one slice) in two stochastic models with density-clumping parameters as for the default model, and different velocity parameters. Dashed: $\delta v/\delta v_\beta = 1$ and $v_j/v_\beta = 0.01$. Solid: $\delta v/\delta v_\beta = -1$ and $v_j/v_\beta = 0.5$ below $v_\beta = 0.6$ and $v_j/v_\beta = 0.15$ above. *Lower:* Corresponding line profiles for a strong line.

be reached. As is clear from Fig. 4, however, this is not the case. This points out two important details not included when deriving the expression for η and interpreting the absorption in terms of this quantity, namely that clumps are distributed randomly (with δt determining only the average distances between them) and that the parameter v_j allows for an asymmetry in the velocities of the clumps' starting points (see Sect. 2.2). These two issues lead to overlapping velocity spans for some of the clumps, whereas for others there is still a velocity gap left between them, through which the radiation can escape. Therefore the profiles do not reach complete saturation, despite that on average $\eta = 0$. This illustrates some inherent limitations when trying to interpret line formation in terms of a simplified quantity such as η.

The impact from the velocity spans of the clumps on the line profiles also depends on the density-clumping parameters. To achieve approximately the same level of absorption, a higher value of $\delta v/\delta v_\beta$ was required in the RHcopy model ($f_v = 0.1$) than in the default model ($f_v = 0.25$), see Fig. 4. Since $\delta v_\beta \propto f_v \delta t$ (see Appendix B), the actual velocity spans of the clumps are different for different density-clumping parameters, even if $\delta v/\delta v_\beta$ remains unchanged.

By changing the sign of δv in the default model (that is, assuming a positive velocity gradient inside the clumps), we have found that our results qualitatively depend only on $|\delta v|$. Some details differ though. For example, a $\delta v > 0$ in our stochastic models permits absorption at velocities higher than the terminal one also within the clumps, whereas $\delta v < 0$ restricts the clump velocities to below the local v_β (see Fig. 2). In this matter v_j plays a role as well, since v_j controls where, with respect to the local v_β, the clumps begin. For reasonable values of v_j, however, its influence is minor on lines where the ICM is insignificant. Finally, tests have confirmed that optically thin lines are only marginally affected when varying $\delta v/\delta v_\beta$.
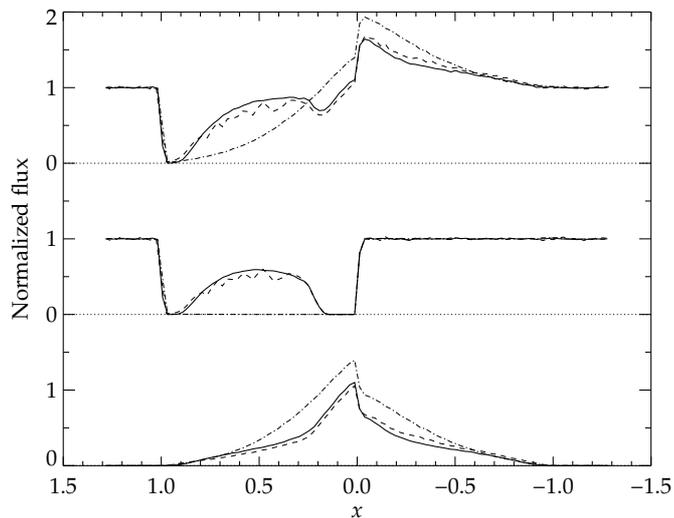
Fig. 9. Total, absorption part, and re-emission part line profiles for 1D, smooth models with $\kappa_0 = 5.0$ (dashed-dotted lines) and $\kappa_0 = 5.0/(2\eta)$ (solid lines, see Sect. 6.1), and for a 2D, stochastic model with density parameters as the default model and a $\beta = 1$ velocity law (dashed lines).

Fig. 10. *Upper panel:* Density structures of one slice in the default stochastic model (upper), in the default stochastic model with a modified δt (middle, see Sect. 6.2), and in FPP (lower). *Lower panel:* Line profiles for the absorption part of an intermediate line for the default model (solid line), for the default model with a modified δt (dashed line), and for the default model with an ionization structure decreasing with increasing velocity (dashed-dotted line, see text).

6. Discussion

6.1. The shapes of the intermediate lines

For intermediate lines, the shape of the absorption part of the default model differs significantly from the shape of a smooth model (see Fig. 4, the middle plot in the lower-left panel). We showed in Sect. 5.1 that the shapes could be qualitatively understood by the behavior of η. This is further demonstrated here by scaling the line strength parameter of a 1D, smooth model, using a parameterization $\kappa_0 \propto \eta^{-1}$ outside the radius $r = 1.3$ where clumping is assumed to start. Fig. 9 displays the line profiles of 1D, smooth models with $\kappa_0 = 5.0$ and $\kappa_0 = 5.0/(2\eta)$. These profiles are compared to those calculated from a 'real' 2D stochastic model with density-clumping parameters as the default model, but with a $\beta = 1$ velocity field. η was calculated from Eq. 7, using the parameters of the default model and a $\beta = 1$ velocity law, and the factor of 2 in the denominator of the scaled κ_0 was chosen so that the *integrated* profile strength of the 2D model was roughly reproduced. From Fig. 9 it is clear that the 1D model with scaled κ_0 well reproduces the 2D results, indicating that indeed η governs the shape of the line profile. We notice also that these profiles display a completely black absorption dip in the outermost wind, as opposed to the default model with a non-monotonic velocity field (see Fig. 4, the middle plot in the lower-left panel). This is because the β velocity field does not allow for any clumps to overlap in velocity space (see the discussion in Sect. 5.3), making the mapping of η almost perfect.

Let us also point out that the line shapes can be somewhat altered by using a different velocity law, e.g., $\beta \neq 1$. Such a change would affect the distances between clumps as well as the Sobolev length, and thereby the line shapes of both absorption and re-emission profiles. However, in all cases is the shape of the re-emission part similar in the clumped and smooth models.

6.2. The onset of clumping and the blue edge absorption dip

We have used $r = 1.3$ as the onset of wind clumping in our stochastic models, which roughly corresponds to the radius where significant structure has developed from the line-driven instability in our RH models. However, Bouret et al. (2003, 2005) analyzed O-stars in the Galaxy and the SMC, assuming optically thin clumps, and found that clumping starts deep in the wind, just above the sonic point. Also Puls et al. (2006) used the optically thin clumping approach, on ρ^2-diagnostics, and found similar results, at least for O-stars with dense winds. With respect to our stochastic models, the qualitative results from Sects. 4 and 5 remain valid when choosing an earlier onset of clumping. Quantitatively, the integrated absorption in intermediate lines becomes somewhat weaker, because the clumping now starts at lower velocities, and of course the line shapes in this region are affected as well. The onset of wind clumping will be important when comparing to observations, as discussed in Sect. 6.6.

The stochastic models that de-saturate an intermediate line generally display an absorption dip toward the blue edge (see Figs. 4 and 9), which has been interpreted in terms of low values of η in the outer wind (see Sect. 5.1). However, this characteristic feature (not to be confused with the so-called DACs, discrete absorption components) is generally not observed, and one may ask whether it might be an artifact of our modeling technique. In the following we discuss two possibilities that may cause our models to overestimate the absorption in the outer wind; the ionization fraction and too low clump separations.

Starting with the former, we have so far assumed a constant ionization factor, $q = 1$ (cf. Eq. A.9). This is obviously an oversimplification. For example, an outwards decreasing q would result in less absorption toward the blue edge. Here we merely demonstrate this general effect, parameterizing $q = v_0/v_\beta$ in the stochastic default model (see Table 2), with $v_0 = 0.1$ the starting point below which $q = 1$. Fig. 10 (lower panel, dashed-dotted

lines) shows how the absorption in the outer wind becomes significantly reduced.

The temperature structure of the wind is obviously important for the ionization balance. Whereas an isothermal wind is assumed in POF (see Sect. 2.1), the FPP model has shocked wind regions with temperatures of several million Kelvin. To roughly map corresponding effects on the line profiles, we re-calculated profiles based on FPP models assuming $q = 0$ in all regions with temperatures higher than $T = 10^5$ K, and $q = 1$ elsewhere. Since the hot gas resides primarily in the low-density regions, however, the emergent profiles were barely affected, and particularly intermediate lines remained unchanged.

On the other hand, the X-ray emission from hot stars (believed to originate in clump-clump collisions, see FPP) is known to be crucial for the ionization balance of highly ionized species such as C IV, N V, and O VI (see, e.g., the discussion in Puls et al. 2008b). X-rays have not been included here, but could in principle have an impact on our line profiles, by illuminating the over-dense regions and thereby changing the ionization balance. Krtička & Kubát (2009), however, find that incorporating X-rays does not influence the PV ionization significantly. Finally, non-LTE analyses including feedback from optically thin clumping have shown that this as well has a significant effect on the derived ionization fractions of, e.g., PV (Bouret et al. 2005; Puls et al. 2008a). To summarize, it is clear that a full analysis of ionization fractions must await a future non-LTE application that includes relevant feedback effects from an inhomogeneous wind on the occupation numbers.

In RH models, the average distance between clumps increases in the outer wind, due to clump-clump collisions and velocity stretching (Feldmeier et al. 1997; Runacres & Owocki 2002). Neglecting the former effect, our stochastic models have clumps much more closely spaced in the outer wind[5]. We have therefore modified the default model by setting $\delta t = 3$ outside a radius corresponding to $v_\beta = 0.7$. This is illustrated in the upper panel of Fig. 10. The mass loss in the new stochastic model is preserved (because the clumps are more extended, see the figure), and this model now better resembles FPP. Recall that differences in the widths of the clumps are expected, since in the default model $f_{cl} \approx f_v^{-1} = 4$, whereas in FPP $f_{cl} \approx 10$. The corresponding line profile shows how the absorption outside $x \approx 0.7$ has been reduced, as expected from the higher δt.

6.3. The velocity spans of the clumps

In Sect. 4.4 it was found that $|\delta v| > \delta v_\beta$ in the RH models. Fig. 11, upper panel, shows the velocity spans of density enhancements (identified as having a density higher than the corresponding smooth value) in the FPP model, and demonstrates that, after structure has developed, $|\delta v|$ is much higher than δv_β throughout the whole wind. These high values essentially stem from the location of the starting points of the density enhancements, which generally lie *before* the velocities have reached their post shock values (see Fig. 11, middle and lower panels). By using a β velocity law (which in principle corresponds to a stochastic velocity law with $v_j = 0$ and $\delta v = \delta v_\beta$, see Fig. 8) together with the density structure from FPP, we simulated a RH wind with low velocity spans. Indeed, for the corresponding intermediate line the equivalent width of the absorption part was $\sim$ 35% lower than that of the original FPP model. The strong line, on the other hand, remained saturated, because the ICM in
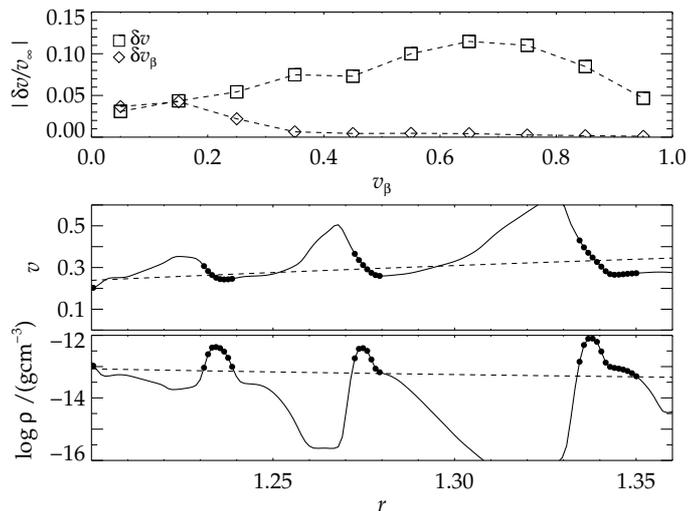
Fig. 11. *Upper:* Velocity spans of density enhancements in the FPP model (squares) and corresponding β intervals (diamonds). *Lower:* Three density enhancements and corresponding velocity spans in the FPP model, highlighted as in Fig. 1.

FPP is not void. So, again, the RH models would in parallel display de-saturated intermediate lines and saturated strong lines, were it not for the large velocity spans inside the clumps.

We suggest that the large velocity span inside a shell (clump) is primarily of kinematic origin, and reflects the formation history of the shell. The shell propagates outwards through the wind, essentially with a $\beta = 1$ velocity law (Owocki et al. 1988). Fast gas is decelerated in a strong reverse shock at the inner rim of the shell. The shell collects ever faster material on its way out through the wind. This new material collected at higher speeds resides on the star-facing side, i.e. at smaller radii, of the slower material collected before. Thus, a negative velocity gradient develops inside the shell. The fact that $|\delta v| \gg \delta v_\beta$ in FPP seems to reflect that the shell is formed at small radii, and then advects outwards maintaining its steep interior velocity gradient[6]. From this formation in the inner, steeply accelerating wind, velocity spans within the shells up to (a few) hundred km s^{-1}, as seen in Fig. 11, appear reasonable.

However, the dynamics of shell formation in hot star winds is very complex due to the creation and subsequent merging of subshells, as caused by nonlinear perturbation growth and the related excitation of harmonic overtones of the perturbation period at the wind base (see Feldmeier 1995). Future work is certainly needed to clarify to which extent the large velocity spans inside the shells in RH models are a stable feature (see also Sect. 7.2).

6.4. 3D effects

A shortcoming of our analysis is the assumed symmetry in Φ. The 2D rather than 3D treatment has in part been motivated by computational reasons (see Appendix A). More importantly though, we do not expect our *qualitative* results to be strongly affected by an extension to 3D. Within the broken-shell wind model, all wind slices are treated independently, and distances between clumps increase only in the radial direction. Therefore

---

[5] The effect is minor in POF, since these RH models only extend to $r \sim 5$ (see Sect. 2.1).

[6] Actually, the velocity gradient may further steepen during advection, due to faster gas trying to overtake slower gas ahead of it; however, this effect is balanced by pressure forces in the subsonic postshock domain.

the expected outcome from extending to 3D is a smoothing effect rather than a reduction or increase in integrated profile strength (similar to the smoothing introduced by N_Θ, see Sect. 4.1). Also, we have shown that the main effect from the inhomogeneous winds is on the absorption part of the line profiles (see, e.g., Sect. 6.1). The formation of this part is dominated by radial photons, especially in the outer wind, because of the dependence only on photons released directly from the photosphere. This implies that most photons stay within their wind slice, restricting the influence from any additional 'holes' introduced by a broken symmetry in Φ to the inner wind. Of course, these expectations hold only within the broken shell model, because in a real 3D wind the clumps will, for example, have velocity components also in the tangential directions.

6.5. Comparison to other studies

To scale the smooth opacity in the formal integral of the non-LTE atmospheric code PoWR, Oskinova et al. (2007) used a porosity formalism in which both f_v and the average distance between clumps enter. Other assumptions were a void ICM, a smooth β velocity field, and a microturbulent velocity $v_t \approx 50\,\mathrm{km\,s^{-1}}$, the last identified as the velocity dispersion within a clump. However, a direct comparison between their study and ours is hampered by the different formalisms used for the spacing of the clumps. Here we have used the 'broken-shell' wind model as a base (see Sect. 2.2), in which each wind slice is treated independently and the distance between clumps increases only in the radial direction (clumps preserve their lateral angles). This gives a radial number density of clumps, $n_{cl} \propto v^{-1}$, the same as used by, e.g., Oskinova et al. (2006), when synthesizing X-ray emission from hot stars. In Oskinova et al. (2007), on the other hand, the distance between clumps increases in *all* spatial directions. In a spherical expansion, this gives a radial number density of clumps $n_{cl} \propto v^{-1}r^{-2}$, i.e., clumps are distributed much more sparsely within this model, especially in the outer wind. Therefore their choice of $L_0 = 0.2$ is not directly comparable with $\delta t = 0.2$ in our models. The shapes of the clumps differ between the two models as well; in Oskinova et al. clumps are assumed to be 'cubes', whereas here the exact shapes of the clumps are determined by the values of the clumping parameters. Despite these differences, our findings confirm the qualitative results of Oskinova et al. that the line profiles become weaker with an increasing distance between clumps as well as with a decreasing v_t. These results may be interpreted on the basis of the effective escape ratio, η (see Eq. 7). Both a decrease in v_t and an increase in the distance between clumps mean that the velocity span covered by a resonance zone becomes smaller when compared to the velocity gap between two clumps (see Fig. 6, left panel), leading to higher probabilities for line photons to escape their resonance zones without interacting with the wind material.

An important result of this paper is that models that desaturate intermediate lines require a non-void ICM to saturate strong lines. This is confirmed by the Oskinova et al. model, in which the ICM is void and strong lines indeed do not saturate (Hamann et al. 2009).

Owocki (2008) proposed a simplified description of the non-monotonic velocity field to account for vorosity, i.e., the velocity gaps between the clumps. Here, the vorosity effect has been discussed using the quantity η (see Sect. 5.1), and we have introduced two new parameters to characterize a non-monotonic velocity field, δv and v_j. The reason for introducing a new parameterization is that when using a single velocity parameter, we have not been able to simultaneously meet the constraints from

strong, intermediate, and weak lines as listed in Sect. 4. Tests using a 'velocity clumping factor' $f_{vel} = \delta v/\Delta v$ as proposed by Owocki (2008), together with a smooth density structure, have shown that this treatment indeed can reduce the line strengths of intermediate lines, but that the observational constraints from strong lines may not be met. Still, the basic concept of vorosity holds within our analysis. For example, one may phrase the high values of δv in the RH models in terms of insufficient vorosity.

6.6. Comparison to observations

We finalize our discussion by performing a first comparison to observations. The two components of the Phosphorus V $\lambda\lambda 1118$-1128 doublet are rather well separated, and the singlet treatment used here suffices to model the major part of the line complex. Nevertheless, the two components overlap within a certain region (indicated in Fig. 12), so when interpreting the results of this subsection, one should bear in mind that the overlap is not properly accounted for, but treated as a simple multiplication of the two profiles.

We used observed FUSE spectra (kindly provided by A. Fullerton) from HD 210839 (λ Cep), a supergiant of spectral type O6 I(n)fp. When computing synthetic spectra, we first assumed optically thin clumping with a constant clumping factor $f_{cl} = 9$ and a smooth $\beta = 1$ velocity field. $f_{cl} = 9$ agrees fairly well with the analysis of Puls et al. (2006), who derived clumping factors $f_{cl} = 6.5$ for $r \approx 1.2\ldots4.0$ and $f_{cl} = 10$ for $r \approx 4.0\ldots15$, assuming an un-clumped outermost wind.[7] We took the ionization fraction $q = q(r)$ of PV from Puls et al. (2008a), calculated with the unified non-LTE atmosphere code FASTWIND for an O6 supergiant, using the Phosphorus model atom from Pauldrach et al. (2001). The feedback from optically *thin* clumping was accounted for and X-rays were neglected. This ionization fraction was then used as input in our MC-1D code when computing the synthetic spectra. We assigned a thermal plus a highly supersonic 'microturbulent' velocity $v_t = 0.05$ (corresponding to 110 km s^{-1}), as is conventional in this approach. The mass-loss rate was derived using the well known relation between κ_0 and $\dot{M}$ (e.g., Puls et al. 2008b). For atomic and stellar parameters, we adopted the same values as in Fullerton et al. (2006).

The dashed line in Fig. 12 represents our fit to the observed spectrum, assuming optically thin clumping, resulting in a mass-loss rate $\dot{M} = 0.24$, in units of $10^{-6}\,\mathrm{M_\odot\,yr^{-1}}$. Fullerton et al. (2006) derived $\langle q \rangle \dot{M} = 0.23$ for this star. Because our clumped FASTWIND model predicts an averaged ionization fraction $\langle q \rangle \approx 0.9$ in the velocity regions utilized by Fullerton et al., the two rates are in excellent agreement. On the other hand, Repolust et al. (2004) for HD 210839 derived $\dot{M} = 6.9$ from H_α assuming an unclumped wind, yielding $\dot{M}_{H_\alpha} = 2.3$ when accounting for the reduction implied by our assumed $f_{cl} = 9$ ($\dot{M}_{H_\alpha} = \dot{M}_{H_\alpha,sm} f_{cl}^{-1/2}$). This rate is almost ten times higher than that inferred from PV, and thus results in PV line profiles that are much too strong (see Fig. 12, dashed-dotted line). That is, to reconcile the H_α and PV rates for HD 210839 with models that assume optically *thin* clumps also in PV, we would have to raise the clumping factor to $f_{cl} > 100$. In addition to this very high clumping factor, the low rate inferred from the PV lines conflicts with the theoretical value $\dot{M} = 3.2$ provided by the mass-

---

[7] This stratification has been found to be prototypical for O-supergiants and was, together with its well developed PV P Cygni profiles, the major reason for choosing λ Cep as comparison object instead of, e.g., ζ Pup, which displays a somewhat unusual run of f_{cl}.

loss recipe in Vink et al. (2000) (using the stellar parameters of Repolust et al. 2004), and is also strongly disfavored by current massive star evolutionary models (Hirschi 2008).

Next we modeled the PV lines using our MC-2D code together with a stochastic 2D wind model. The same clumping factor (f_{cl} = 9) and ionization fraction (calculated from FASTWIND, see above) were used. This time, we assigned v_t = 0.005, i.e., applied no microturbulence. In previous sections, e.g. 4.3 and 6.1, we showed that stochastic models generally display a line shape different from smooth models, with a characteristic absorption dip at the blue edge as well as a dip close to the line center. Such shapes are not seen in the PV lines in λ Cep. Thus, to better resemble the observed line shapes, we used different values for δt and x_{ic} in the inner and outer wind (the former modification already discussed in Sect. 6.2) and let clumping start close to the wind base. Clumping parameters are given in Table 2, model Obs1.

As illustrated in Fig. 12, the synthetic line profiles using $\dot{M}$ = 2.3, as inferred from H_α, are now at the observed levels. Because of our insufficient treatment of line overlap, we gave higher weight to the λ1118 component when performing the fitting, but the profile-strength ratio between the blue and red component was nevertheless reasonably well reproduced (see also discussion in Sect. 5.2). However, though the fit appears quite good, we did not aim for a perfect one, and must remember the deficits of our modeling technique. For example, while the early onset of clumping definitely improved the fit (using our default value, there was a dip close to line center) and might be considered as additional evidence that clumping starts close to the wind base, the same effect could in principle be produced by non-LTE effects close to the photosphere or by varying the underlying β velocity law. Such effects will be thoroughly investigated in a follow-up paper, which will also include a comparison to observations from many more objects.

Clearly, a consistent modeling of resonance lines (at least of intermediate strengths) requires the consideration of a much larger parameter set than if modeling via the standard diagnostics assuming optically thin clumping, and a reasonable fit to a single observed line complex can be obtained using a variety of different parameter combinations. The analysis of PV lines as done here can therefore, at present, only be considered as a consistency check for mass-loss rates derived from other, independent diagnostics, and not as a tool for directly estimating mass-loss rates. Additional insight might be gained by exploiting more resonance doublets, due to the different reactions of profile strengths and shapes on κ_0. The different slopes of the equivalent width as a function of κ_0 in smooth and clumped models, especially at intermediate line strengths (Sect. 5.2), may turn out to be decisive. However, because of, e.g., the additional impact from the ICM density, also this diagnostics requires additional information from saturated lines. Taken together, only a consistent analysis using different diagnostics and wavelength bands, and embedded in a suitable non-LTE environment, will (hopefully) provide a unique view.

7. Summary and future work

7.1. Summary

Below we summarize our most important findings:

- When synthesizing resonance lines in inhomogeneous hot star winds, the detailed density structure, the non-monotonic velocity field, and the inter-clump medium are all important
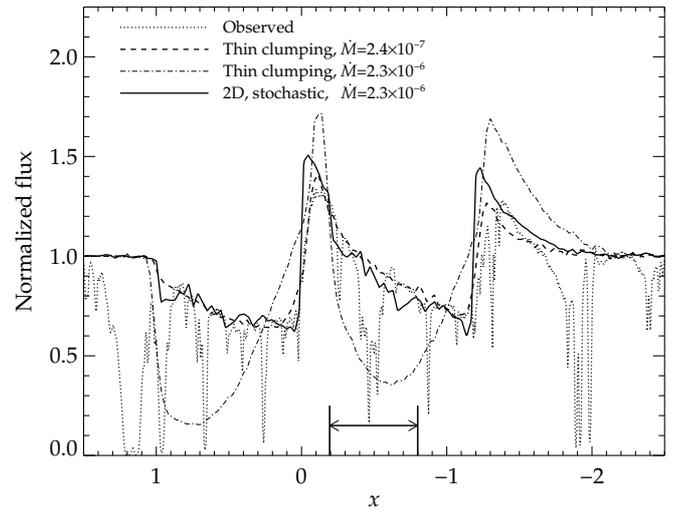
Fig. 12. Observed FUSE spectra of the PV doublet $\lambda\lambda$1118-1128 for the O6 supergiant λ Cep (Fullerton et al. 2006). The synthetic spectra are calculated for two 1D models assuming optically thin clumping (see Sect. 6.6) and for one 2D stochastic model with parameters as in Table 2, model Obs1. The models have mass-loss rates $\dot{M}$ [$M_\odot$ yr^{-1}] as given in the figure. The zero point frequency is shifted to the line center of the λ1118 component, and the two arrows at the bottom of the figure indicate in which region the two components overlap.

for the line formation. Adequate models must be able to simultaneously meet observational and theoretical constraints from strong, intermediate, and weak lines.

- Resonance lines are basically unaffected by the inhomogeneous wind structure in the limit of optically thin clumps, but the clumps remain optically thin only for very weak lines.
- We confirm the basic effects of porosity (stemming from optically thick clumps) and vorosity (stemming from velocity gaps between the clumps) in the formation of primarily lines of intermediate strengths.
- We point out the importance of a non-void ICM for the simultaneous formation of strong and intermediate lines that meet observational constraints.
- Porosity and vorosity are found to be intrinsically coupled and of similar importance. To characterize their mutual effect on intermediate lines, we have identified a crucial parameter, the 'effective escape ratio', that describes to which extent photons may escape their resonance zones without ever interacting with the wind material.
- We confirm previous results that time-dependent, radiation-hydrodynamic wind models reproduce observed characteristics for strong lines, without applying the highly supersonic microturbulence needed in smooth models.
- A significant profile strength reduction of intermediate lines (as compared to smooth models) is for the radiation-hydrodynamic models prevented by the large velocity spans of the density enhancements, implying that the wind structures predicted by present day RH models are not able to reproduce the observed strengths of intermediate lines unless invoking a very low mass-loss rate.
- Provided a non-void ICM and not too large velocity spans inside the clumps, 2D *stochastic* wind models saturate strong lines, while simultaneously not saturating intermediate lines (that are saturated in smooth models). Using typical volume filling factors, $f_v \approx 0.25$, the resulting integrated profile

strength reductions imply that these inhomogeneous models would be compatible with mass loss rates roughly a factor of ten higher than those derived from resonance lines using smooth models.

– A first comparison to observations was made for the O6 supergiant λ Cep. It was found that, indeed, the line profiles of PV based on a 2D stochastic wind model, accounting for a detailed density structure and a non-monotonic velocity field, reproduced the observations with a mass-loss rate almost ten times higher than the rate derived from the same lines, but with a model that used the optically thin clumping approach. This alleviated the discrepancies between theoretical predictions, evolutionary constraints, and previous mass-loss rates based on winds assumed either to be smooth or to have optically thin clumps.

7.2. Future work

We have investigated general properties of resonance line formation in inhomogeneous 2D wind models with non-monotonic velocity fields. To perform a detailed and quantitative comparison to observations, and derive mass-loss rates, simplified approaches need to be developed and incorporated into non-LTE models to obtain reliable occupation numbers. Extending our Monte-Carlo radiative transfer code to include line overlap effects in doublets is critical for more quantitative applications, and an extension to 3D is also necessary. Further applications involve synthesizing emission lines, for example to test the optically thin clumping limit both in the parameter range where this is thought to be appropriate (e.g., for O-/early B-stars), and in other more complicated situations. Indeed, the present generation of line-blanketed model atmospheres does not seem to be able to reproduce H_α line profiles from A-supergiants, which are observed as P-Cygni profiles with *non-saturated* troughs, whereas the simulations (assuming optically thin clumping) result in saturated troughs (R.-P. Kudritzki, private communication). Since H_α is a quasi-resonance line and not a recombination line in these cooler winds (e.g., Kudritzki & Puls 2000), this behavior might be explained by the presence of optically thick clumps.

Finally, it needs to be clarified if the large velocity span inside clumps generated in RH models is independent of additional physics that is not, or only approximately, accounted for in present simulations (such as more-D effects and/or various exciting mechanisms). If the large velocity span is a stable feature, one might come to the (rather unfortunate) conclusion that either the observed clumping features are not, or only weakly, related to the line-driven instability, or the discrepancies between observed and synthetic flux distribution (from the X-ray to the radio regime) might involve processes different from the present paradigm of wind clumping.

References

Abbott, D. C., Bieging, J. H., & Churchwell, E. 1981, ApJ, 250, 645
Bouret, J.-C., Lanz, T., & Hillier, D. J. 2005, A&A, 438, 301
Bouret, J.-C., Lanz, T., Hillier, D. J., et al. 2003, ApJ, 595, 1182
Busche, J. R. & Hillier, D. J. 2000, ApJ, 531, 1071

Castor, J. I. 1970, MNRAS, 149, 111
Castor, J. I., Abbott, D. C., & Klein, R. I. 1975, ApJ, 195, 157
Crowther, P. A., Hillier, D. J., Evans, C. J., et al. 2002, ApJ, 579, 774
Dessart, L. & Owocki, S. P. 2002, A&A, 383, 1113
Dessart, L. & Owocki, S. P. 2003, A&A, 406, L1
Dessart, L. & Owocki, S. P. 2005, A&A, 437, 657
Eversberg, T., Lepine, S., & Moffat, A. F. J. 1998, ApJ, 494, 799
Feldmeier, A. 1995, A&A, 299, 523
Feldmeier, A., Oskinova, L., & Hamann, W.-R. 2003, A&A, 403, 217
Feldmeier, A., Puls, J., & Pauldrach, A. W. A. 1997, A&A, 322, 878
Fullerton, A. W., Massa, D. L., & Prinja, R. K. 2006, ApJ, 637, 1025
Gräfener, G., Koesterke, L., & Hamann, W.-R. 2002, A&A, 387, 244
Hamann, W. ., Graefener, G., Oskinova, L. M., & Feldmeier, A. 2009, ArXiv e-prints
Hamann, W.-R. 1981, A&A, 93, 353
Hamann, W.-R., Feldmeier, A., & Oskinova, L. M., eds. 2008, Clumping in hot-star winds
Hillier, D. J. & Miller, D. L. 1998, ApJ, 496, 407
Hirschi, R. 2008, in Clumping in Hot-Star Winds, ed. W.-R. Hamann, A. Feldmeier, & L. M. Oskinova, 9–+
Krtička, J. & Kubát, J. 2009, MNRAS, 394, 2065
Kudritzki, R.-P. & Puls, J. 2000, ARA&A, 38, 613
Lamers, H. J. G. L. M., Cerruti-Sola, M., & Perinotto, M. 1987, ApJ, 314, 726
Lépine, S. & Moffat, A. F. J. 2008, AJ, 136, 548
Lucy, L. B. 1983, ApJ, 274, 372
Lucy, L. B. & Solomon, P. M. 1970, ApJ, 159, 879
Massa, D. L., Prinja, R. K., & Fullerton, A. W. 2008, in Clumping in Hot-Star Winds, ed. W.-R. Hamann, A. Feldmeier, & L. M. Oskinova, 147–+
Meynet, G., Maeder, A., Schaller, G., Schaerer, D., & Charbonnel, C. 1994, A&AS, 103, 97
Mihalas, D., Kunasz, P. B., & Hummer, D. G. 1975, ApJ, 202, 465
Oskinova, L. M., Feldmeier, A., & Hamann, W.-R. 2004, A&A, 422, 675
Oskinova, L. M., Feldmeier, A., & Hamann, W.-R. 2006, MNRAS, 372, 313
Oskinova, L. M., Hamann, W.-R., & Feldmeier, A. 2007, A&A, 476, 1331
Owocki, S. P. 2008, in Clumping in Hot-Star Winds, ed. W.-R. Hamann, A. Feldmeier, & L. M. Oskinova, 121–+
Owocki, S. P., Castor, J. I., & Rybicki, G. B. 1988, ApJ, 335, 914
Owocki, S. P., Gayley, K. G., & Shaviv, N. J. 2004, ApJ, 616, 525
Owocki, S. P. & Rybicki, G. B. 1984, ApJ, 284, 337
Pauldrach, A., Puls, J., & Kudritzki, R. P. 1986, A&A, 164, 86
Pauldrach, A. W. A., Hoffmann, T. L., & Lennon, M. 2001, A&A, 375, 161
Puls, J., Markova, N., & Scuderi, S. 2008a, in Astronomical Society of the Pacific Conference Series, Vol. 388, Mass Loss from Stars and the Evolution of Stellar Clusters, ed. A. de Koter, L. J. Smith, & L. B. F. M. Waters, 101–+
Puls, J., Markova, N., Scuderi, S., et al. 2006, A&A, 454, 625
Puls, J., Owocki, S. P., & Fullerton, A. W. 1993, A&A, 279, 457
Puls, J., Urbaneja, M. A., Venero, R., et al. 2005, A&A, 435, 669
Puls, J., Vink, J. S., & Najarro, F. 2008b, A&A Rev., 16, 209
Repolust, T., Puls, J., & Herrero, A. 2004, A&A, 415, 349
Runacres, M. C. & Owocki, S. P. 2002, A&A, 381, 1015
Rybicki, G. B. & Hummer, D. G. 1978, ApJ, 219, 654
Smith, N. & Owocki, S. P. 2006, ApJ, 645, L45
Vink, J. S., de Koter, A., & Lamers, H. J. G. L. M. 2000, A&A, 362, 295
Zsargó, J., Hillier, D. J., Bouret, J.-C., et al. 2008, ApJ, 685, L149

Appendix A: The Monte-Carlo transfer code

A.1. The code

Here we describe our Monte-Carlo radiative transfer code (MC-2D) in some detail. For an overview of basic assumptions, see Sect. 3 in the main paper. For testing purposes, versions to treat spherically symmetric winds, either in the Sobolev approximation (MCS-1D) or exactly (MC-1D), have been developed as well.

Geometry. For wind models in which the spherical symmetry is broken, we can no longer restrict photon trajectories to rays with constant impact parameters (see below). Moreover, the observed spectrum will depend on the observer's placement relative to the star. Fig. A.1 illustrates the geometry in use, a standard right-handed spherical system (r, Θ, Φ) defined relative to a Cartesian

set (X, Y, Z) (transformations between the two may be found in any standard mathematical handbook). At each coordinate point we also construct a local coordinate system using the local unit vectors (r_u, Θ_u, Φ_u), which for a photon propagating in direction n_u is related to the *radiation coordinates* (θ, ϕ) (see Fig. A.1) via

$$\cos \theta \equiv \mu = r_u \cdot n_u, \tag{A.1}$$

$$\sin \phi \sin \theta = \Phi_u \cdot n_u = \frac{Z_u \times r_u}{|Z_u \times r_u|} \cdot n_u, \tag{A.2}$$

$$\cos \phi \sin \theta = \Theta_u \cdot n_u = [\Phi_u \times r_u] \cdot n_u. \tag{A.3}$$

The radiation coordinates are defined on the intervals $\theta = 0 \ldots \pi$ and $\phi = 0 \ldots 2\pi$, but due to the symmetry in Φ, only the range $\phi = 0 \ldots \pi$ needs to be considered (see Busche & Hillier 2000). Also, for this symmetry, the direction cosines of n_u simplify to

$$n_x = \mu \sin \Theta + \sqrt{1 - \mu^2} \cos \phi \cos \Theta, \tag{A.4}$$

$$n_y = \sqrt{1 - \mu^2} \sin \phi, \tag{A.5}$$

$$n_z = \mu \cos \Theta - \sqrt{1 - \mu^2} \cos \phi \sin \Theta. \tag{A.6}$$

Eqs. A.1-A.6 are used to update the physical position (r, Θ) of the photon and the local values of the radiation coordinates (θ, ϕ). By tracking the photon on a radial mesh, both the physical and radiation coordinates can be updated exactly. Interpolations are necessary only when a photon is scattered or when it crosses a Θ-boundary to another wind slice. Essentially the same coordinate system is used by, e.g., Busche & Hillier (2000). We collect escaped photons according to their Θ-angles at 'infinity'[8], and bin them using the same N_Θ bins as in the underlying wind model (see Sect. 2).

For spherically symmetric wind models, we adhere to the customary (p, z) spatial coordinate system with p being the impact parameter and z the direction toward the observer. Each time a photon is scattered and its direction determined, a new impact parameter is computed from the relation $p = r\sqrt{(1 - \mu^2)}$, appreciating that all points on a surface of constant radius can be treated equally in this geometry.

Releasing photons. We release photons from the lower boundary uniformly in ϕ and with a distribution function $\propto \mu d\mu$ in μ (e.g., Lucy 1983). The angular coordinate Θ is selected so that photons are uniformly distributed over the surface area $dA = \sin \Theta d\Theta d\Phi$.

Absorption. The probability of photon absorption is $\propto e^{-\tau} d\tau$, hence the optical depth τ the photon travels before absorption can be selected according to $\tau = -\ln R_1$, where R_1 is a random number between 0 and 1. The position for absorption in the wind may then be determined by inverting the line optical depth integral along the photon path

$$\tau_\nu = \int \chi_\nu ds, \tag{A.7}$$

with the frequency-dependent opacity

$$\chi_\nu = \kappa_L \rho \phi_\nu, \tag{A.8}$$

<hr>

[8] The full 3D problem would require binning in Φ as well, which in turn would require a large increase in the number of simulated photons.
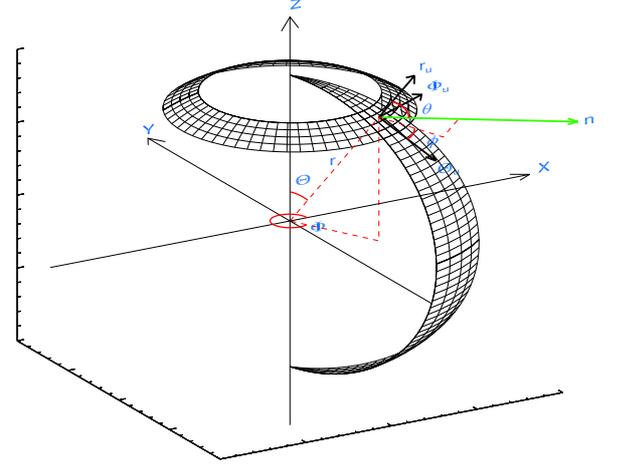
Fig. A.1. Illustration of the coordinate system, see text. *A color version of this figure is available in the web version.*

with ϕ_ν the absorption profile, κ_L the frequency integrated mass absorption coefficient, and ρ the mass density. All dependencies on spatial location are for simplicity suppressed here and in the following. For the opacity we use the parameterization from Hamann (1981) and POF,

$$\kappa_L \lambda \rho = \frac{4\pi R_\star v_\infty^2}{\dot{M}} \kappa_0 \rho q, \tag{A.9}$$

where λ is the wavelength of the considered transition, κ_0 is a 'line-strength' parameter taken to be constant, $\dot{M}$ the radially and laterally averaged mass-loss rate, and $q = q(r, \Theta)$ the fraction of the considered element that resides in the investigated ionic stage. Default here is $q = 1$, but effects from other ionization structures are discussed in Sect. 6.2. κ_0 is proportional to the product of mass-loss rate and abundance of the considered ion, and, for a smooth wind, $\kappa_0 = 1$ and $\kappa_0 = 100$ give a typical medium and strong line, respectively. The parameterization as defined in Eq. A.9 has the advantage that for smooth winds the radial optical depth in the Sobolev approximation collapses to

$$\tau_{Sob} = \frac{\kappa_0}{r^2 v dv/dr} q, \tag{A.10}$$

when v and r are expressed in normalized units. The corresponding expression for clumpy winds is provided in Eq. 5. The absorption profile is assumed to be a Gaussian with a Doppler width v_t that contains the contributions from thermal and (if present) 'microturbulent' velocities. To solve Eq. A.7, we adopt the dimensionless frequency x with the terminal velocity of a smooth outflow as the reference speed,

$$x = \frac{\nu - \nu_0}{\nu_0} \frac{c}{v_\infty}, \tag{A.11}$$

and transform to the co-moving frame (hereafter CMF). ν_0 is the rest-frame frequency of the line center and c the speed of light. We now assume that between two grid points the variation of the factor $\kappa_L \rho / |Q|$ (see below) is small and may be replaced by an average value. The optical depth $\Delta\tau_\nu$ between two subsequent spatial points (r, Θ) then becomes

$$\Delta\tau_\nu = \left| \frac{\lambda R_\star}{v_\infty} \frac{\kappa_L \rho}{Q} \times \frac{-\Delta \text{erf}[x_{cmf}/v_t]}{2} \right|, \tag{A.12}$$

where Δerf is the difference of the error-function between the points, x_{cmf} the dimensionless CMF frequency, and v_t is calculated in units of v_∞. $Q \equiv n_u \cdot \nabla (n_u \cdot v)$ is the local directional derivative of the velocity in direction n_u, with velocities measured in units of v_∞ and radii in units of $R_\star$. By interpolating to the border whenever a photon crosses a Θ boundary, we *locally* recover the spherically symmetric expression

$$Q = \frac{\partial v}{\partial r}\mu^2 + \frac{v}{r}(1 - \mu^2). \qquad (A.13)$$

For spherically symmetric winds, we have written a second implementation that allows for line transfer using the Sobolev approximation. With this method each resonance zone is approximated by a point and the line only collects optical depth at atmospheric locations where the observer's frame frequency x_{obs} has been Doppler shifted to coincide with the CMF frequency for the line center. The condition for interaction thus is $x_{obs} = \mu v$ and the last factor in Eq. A.12 collapses to unity when calculating the Sobolev optical depth. The Sobolev approach can be expected a reasonable approximation when the variation of the factor $\kappa_L\rho/|Q|$ is small within the whole resonance zone contributing to the optical depth in Eq. A.12, i.e., small on length scales at least a few times the Sobolev length $L \equiv v_t/|Q|$. However, also in the Sobolev approximation more than one resonance point may be identified in a wind with a non-monotonic velocity field.

Re-emission. We assume complete redistribution and isotropic re-emission in the CMF, allowing for a multitude of scattering events within one resonance zone. When the Sobolev approximation is applied, re-emission is assumed to be coherent in the CMF and for the angular re-distribution we then use the corresponding escape probabilities (Castor 1970), corrected for a treatment of negative velocity gradients (Rybicki & Hummer 1978; POF). In this case, there is only one effective scattering event inside the localized resonance zone.

After the photon has been re-emitted at some atmospheric location, the procedure runs again and searches for another absorption.

A.2. Radiative transfer code tests

In this subsection we describe some of the verification tests of our MC radiative transfer code that we have made. The MC-1D version was first applied on spherically symmetric winds, comparing profiles from smooth, stationary winds to profiles calculated using the well-established CMF (cf. Mihalas et al. 1975; Hamann 1981) and SEI methods, and profiles from time-dependent RH winds to profiles calculated using the Sobolev method developed in POF. Thereafter we applied the MC-2D version on models in which all lateral slices had the same radial structure, comparing the results to the MC-1D version.

First we calculated line profiles for smooth, 1D winds. We have verified that for low[9] values of v_t, profiles from all the methods described above agree perfectly, whereas for higher values the MC-1D and CMF give identical results but the SEI deviates significantly, especially for a medium-strong line (see Fig. A.2, upper panel). This is due to the hybrid nature of the SEI technique, which approximates the source function with its local Sobolev value but carries out the exact formal integral. Because of this, the method does not account for the increasing amount of
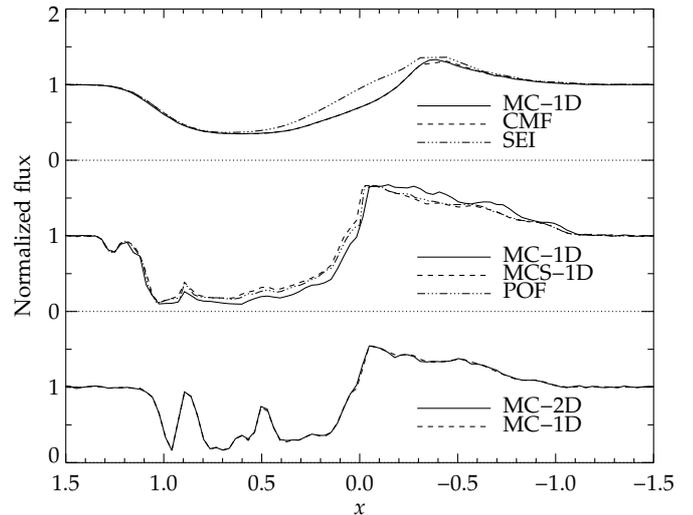
Fig. A.2. Synthetic line profiles for spherically symmetric models, calculated with the labeled methods. Profiles are shown for a smooth model with $\kappa_0 = 1.0$ and $v_t = 0.2$ (upper) and for two POF snapshots with $\kappa_0 = 100$ (middle) and $\kappa_0 = 5.0$ (lower) and $v_t = 0.005$. The 2D profile is for an observer at the equator. x is the normalized observer's frame frequency (see Eq. A.11), and the ordinate displays the emergent flux normalized to the continuum flux.

photons close to line center that are backscattered into the photosphere when the resonance zone grows and overlaps with the lower boundary.[10] Consequently the re-emitted flux in this region is higher when calculated via the SEI than when calculated via the CMF or MC methods. These discrepancies between the CMF and SEI are quite well documented and discussed (e.g., Hamann 1981; Lamers et al. 1987), however we still emphasize that one should exercise caution when applying the SEI method with high microturbulence on wind resonance lines. Especially today, when increased computer-power enables us to compute fast solutions using both methods, the CMF is preferable.

Next we calculated line profiles for structured, 1D winds. Profiles computed with all three methods agreed for weak and intermediate lines. For strong lines, the agreement between MCS-1D and the method from POF, which uses a Sobolev source function accounting for multiple-resonance points, was satisfactory. However, minor discrepancies between Sobolev and non-Sobolev treatments occurred for the strong line also when no microturbulent velocity was applied (see Fig. A.2), as opposed to the smooth case.

Finally we performed a simple test of our MC-2D code by applying it on models in which all lateral slices had the same radial structure, i.e., the wind was still spherically symmetric and all observers ought to see the same spectrum. We confirmed that indeed so was the case, both for smooth and structured models (in Fig. A.2 the latter case is demonstrated).

---

[9] For a typical terminal velocity value $v_\infty = 2000$ km s^{-1}, $v_t = 0.005$ corresponds to 10 km s^{-1} and $v_t = 0.2$ to 400 km s^{-1}.

[10] Remember that neither the SEI nor the CMF, as formulated here, include a transition to the photosphere, but treat the lower boundary as sharp with a minimum velocity v_{min}.

Appendix B: The effective escape ratio

We define the ratio of the velocity gap Δv between two clumps (see Fig. 6 in the main paper) and the thermal velocity v_t as

$$\eta \equiv \frac{\Delta v}{v_t}. \tag{B.1}$$

In the following, we derive an expression for η, for the wind geometry used throughout this paper. If $\Delta v_{tot} = \Delta v + |\delta v|$ is the velocity difference between two clump *centers*, we may write (omitting the absolute value signs here and in the following)

$$\Delta v = \Delta v_{tot} - \delta v = \frac{\Delta v_{tot}}{\Delta v_{tot,\beta}} \Delta v_{tot,\beta} - \frac{\delta v}{\delta v_\beta} \delta v_\beta, \tag{B.2}$$

where we have normalized the arbitrary velocity intervals to the corresponding β intervals. β suffixes are used to denote parameters of a smooth velocity law. For notational simplicity we write

$$\xi_1 = \frac{\Delta v_{tot}}{\Delta v_{tot,\beta}}, \qquad \xi_2 = \frac{\delta v}{\delta v_\beta}. \tag{B.3}$$

Assuming radial photons, Δv may be approximated by

$$\Delta v \approx \frac{\partial v_\beta}{\partial r} \Delta r_{tot,\beta} (\xi_1 - \xi_2 \frac{\delta r_\beta}{\Delta r_{tot,\beta}}), \tag{B.4}$$

with the notations of r following those of v. The volume filling factor for the geometry in use is

$$f_v \equiv \frac{V_{cl}}{V_{tot}} \approx \frac{r_1^2 \delta r}{r_2^2 \Delta r_{tot}} \tag{B.5}$$

with V_{cl} the volume of the clump, V_{tot} the total volume, and $r_1 \approx r_2$ the radial points associated with the beginning of the clump and the ICM. Using Eq. B.5 and $\Delta r_{tot} = v_\beta \delta t$ (see Sect. 2.2), we obtain

$$\Delta v \approx \frac{\partial v_\beta}{\partial r} v_\beta \delta t (\xi_1 - \xi_2 f_v), \tag{B.6}$$

and for η, using the radial Sobolev length of a smooth flow $L_r = v_t/(\partial v_\beta/\partial r)$,

$$\eta \approx \frac{v_\beta \delta t (\xi_1 - \xi_2 f_v)}{L_r}. \tag{B.7}$$

In our models ξ_1 is not given explicitly, but is on the order of unity, because we distribute clumps according to the underlying smooth $\beta = 1$ velocity law. Thus we approximate

$$\eta \approx \frac{v_\beta \delta t (1 - \xi_2 f_v)}{L_r}. \tag{B.8}$$

We notice that the porosity length h as defined by Owocki et al. (2004) is $h = l/f_v$, where l is the length associated with the clump. For the geometry used here this becomes $h \approx \delta r/f_v \approx v_\beta \delta t$. Hence, using $\xi_2 = 1$ for a smooth velocity field, η represents the porosity length corrected for the finite size of the clump, and divided by the radial Sobolev length.